ФИЗИКА ЭЛЕМЕНТАРНЫХ ЧАСТИЦ И АТОМНОГО ЯДРА
2016. Т. 47. ВЫП. 4

FEASIBILITY STUDY OF HEAVY ION PHYSICS PROGRAM AT NICA

P. N. Batyuk [1,*], *V. D. Kekelidze* [1], *V. I. Kolesnikov* [1],
O. V. Rogachevsky [1], *A. S. Sorin* [1,2], *V. V. Voronyuk* [1]
on behalf of the BM@N and MPD collaborations

[1] Joint Institute for Nuclear Research, Dubna
[2] National Research Nuclear University
"Moscow Engineering Physics Institute" (MEPhI), Moscow

*E-mail: pavel.batyuk@jinr.ru

ФИЗИКА ЭЛЕМЕНТАРНЫХ ЧАСТИЦ И АТОМНОГО ЯДРА
2016. Т. 47. ВЫП. 4

FEASIBILITY STUDY OF HEAVY ION PHYSICS PROGRAM AT NICA

P. N. Batyuk [1,*], *V. D. Kekelidze* [1], *V. I. Kolesnikov* [1], *O. V. Rogachevsky* [1], *A. S. Sorin* [1,2], *V. V. Voronyuk* [1]
on behalf of the BM@N and MPD collaborations

[1] Joint Institute for Nuclear Research, Dubna
[2] National Research Nuclear University "Moscow Engineering Physics Institute" (MEPhI), Moscow

There is strong experimental and theoretical evidence that in collisions of heavy ions at relativistic energies the nuclear matter undergoes a phase transition to the deconfined state — Quark–Gluon Plasma. The caused energy region of such a transition was not found at high energy at SPS and RHIC, and search for this energy is shifted to lower energies, which will be covered by the future NICA (Dubna), FAIR (Darmstadt) facilities and BES II at RHIC. Fixed target and collider experiments at the NICA facility will work in the energy range from a few A GeV up to $\sqrt{s_{NN}} = 11$ GeV and will study the most interesting area on the nuclear matter phase diagram.

The most remarkable results were observed in the study of collective phenomena occurring in the early stage of nuclear collisions. Investigation of the collective flow will provide information on Equation of State (EoS) for nuclear matter. Study of the event-by-event fluctuations and correlations can give us signals of critical behavior of the system. Femtoscopy analysis provides the space-time history of the collisions. Also, it was found that baryon stopping power revealing itself as a "wiggle" in the excitation function of curvature of the (net) proton rapidity spectrum relates to the order of the phase transition.

The available observations of an enhancement of dilepton rates at low invariant masses may serve as a signal of the chiral symmetry restoration in hot and dense matter. Due to this fact, measurements of the dilepton spectra are considered to be an important part of the NICA physics program. The study of strange particles and hypernuclei production gives additional information on the EoS and "strange" axis of the QCD phase diagram.

In this paper a feasibility of the considered investigations is shown by the detailed Monte Carlo simulations applied to the planned experiments (BM@N, MPD) at NICA.

Существуют убедительные экспериментальные и теоретические свидетельства в пользу того, что в столкновениях тяжелых ионов при релятивистских энергиях ядерная материя претерпевает фазовый переход и переходит в состояние кварк-глюонной

*E-mail: pavel.batyuk@jinr.ru

плазмы. Энергетический диапазон, при котором осуществляется подобный переход, не был обнаружен при высоких энергиях на SPS и RHIC. По этой причине предполагается продолжить поиск в области более низких энергий в рамках планируемых экспериментов на ускорительном комплексе NICA (Дубна, Россия), FAIR (Дармштадт, Германия) и BES II на RHIC (США). Эксперименты на фиксированной мишени, наряду с экспериментами на встречных пучках на ускорительном комплексе NICA, будут проводиться для тяжелых ядер в энергетическом диапазоне, начиная от нескольких ГэВ вплоть до 11 ГэВ на нуклон в системе центра масс сталкивающихся ядер, позволяя изучать наиболее интересную область на фазовой диаграмме ядерной материи.

Наиболее значимые результаты были получены при изучении коллективных явлений, происходящих на ранней стадии ядерных столкновений. Исследование коллективных потоков позволяет получить информацию об уравнении состояния ядерной материи. Изучение пособытийных флуктуаций и корреляций дает сигналы о критическом поведении системы. Анализ, выполненный средствами фемтоскопии, позволяет получить пространственно-временную историю столкновения. Также было выявлено, что тормозящая способность вещества для барионов (baryon stopping power), обнаруживающаяся в нерегулярном поведении кривизны в спектре распределения $p\bar{p}$ по быстроте, связана с порядком фазового перехода.

Имеющиеся наблюдения в пользу увеличения выхода дилептонов при малых инвариантных массах могут служить в качестве сигнала восстановления киральной симметрии в горячей и плотной ядерной материи. По этой причине измерения дилептонных спектров являются важными в рамках физической программы экспериментов на ускорительном комплексе NICA. Изучение странных частиц и образования гиперъядер дает дополнительную информацию об уравнении состояния ядерной материи и «странной» оси на фазовой диаграмме.

В данной работе посредством моделирования методом Монте-Карло обосновывается возможность реализации рассмотренных выше исследований применительно к планирующимся на ускорительном комплексе NICA экспериментам (BM@N и MPD).

PACS: 25.75.-q; 25.70.Bc; 25.70.Jj

INTRODUCTION

The main goal of the physics program at the Nuclotron-based Ion Collider fAcility (NICA) accelerator complex is a search for the mixed phase of quark matter and baryon-rich hadronic matter as a consequence of the first-order phase transition. It has to be emphasized that the current view of the QCD phase diagram (Fig. 1) is mostly an artistic view with only a few quantitative details from the available experimental data or some QCD simulations on it. In the era of NICA this situation shall change and experimental data shall draw the QCD landscape [1]. There is strong experimental evidence that the deconfined phase

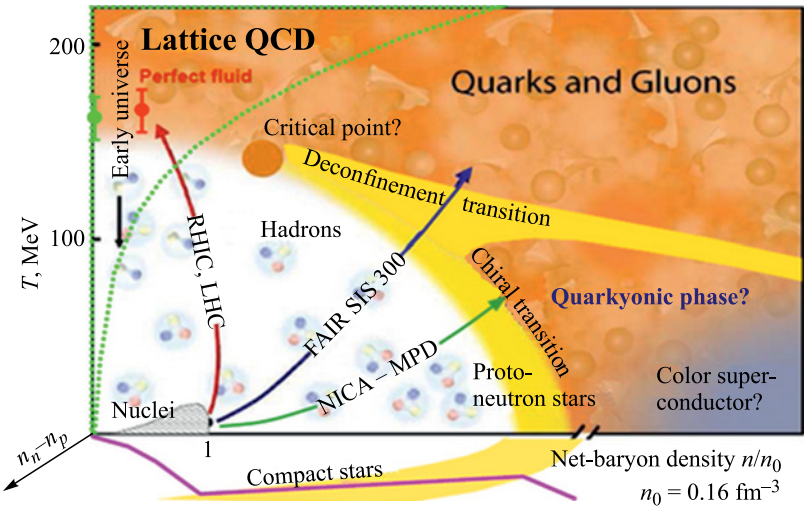

Fig. 1. The three-dimensional QCD phase diagram. The regions that can be accessed by heavy-ion collisions at different energies are indicated

of nuclear matter — Quark–Gluon Plasma (QGP) — can be created in ultra-high-energy nuclear collisions [2–5]. As the collision energy is being decreased down to several GeV per nucleon–nucleon pair, there is a certain transition region of the collision energy below which it is no longer possible to access the plasma phase in the course of the collision. The existing data on single-particle spectra and mean multiplicities [6] suggest that the transition occurs within the NICA energy range ($4 \leqslant \sqrt{s_{NN}} \leqslant 11$ GeV). Moreover, the chosen NICA energy range is sufficient to encompass both: collisions in which the plasma phase is well developed and collisions in which the matter remains in a purely hadronic phase. Thus, NICA is ideally suited for exploring the transition between the familiar hadronic phase and the new plasma phase.

Theoretical understanding of the transition between the hadronic phase and the plasma phase, and how it manifests itself in the nuclear collision observables, is still rather poor, and quantitative predictions cannot yet be made with confidence. In particular, the lattice gauge calculations cannot presently be employed at the finite baryon densities which will be studied by NICA. Furthermore, in addition to determining the existence and location of the transition region, where the new plasma phase is being created at the beginning, it is of fundamental interest to establish a character of the associated phase transformation, whether it remains a smooth crossover, or becomes a first-order transition, as many models predict. In the latter case, the phase diagram of the strongly interacting matter must contain a critical point and its experimental identification forms a focal point for this

research field. Therefore, it has been suggested [1] that the first round of the NICA experiments should concentrate on a variety of diagnostic observables that have already been employed in experimental programs at RHIC and SPS.

The observables include particle yields and spectra, the event-by-event fluctuations of multiplicity and transverse momentum of charged particles and the identified particles (p, K, π, Λ and their antiparticles) as well as the corresponding joint distributions. Possible measurements should be carried out as a function of the collision energy for many systems including the elementary ($p+p$, $d+d$ and $d+A$) reactions and collisions of nuclei of intermediate mass and heavy ions (up to gold). In consequence of these measurements, freeze-out conditions will be precisely established for the collisions in the transition domain. In the second stage one should consider measurements of open-charm hadrons, dileptons and diphotons.

NICA will be a new accelerator complex being constructed at JINR aimed to provide collider experiments with heavy ions up to gold at the maximum energy $\sqrt{s_{NN}} = 11$ GeV. The proposed facility (Fig. 2) consists of:

1. Electron string ion source that provides Au^{79+} ions at an intensity of $2 \cdot 10^9$ ions per pulse of about 7 μs duration at a repetition rate of up to 50 Hz.

2. Injector on the basis of a linear accelerator consisting of the Drift Tube Linac sections. The linac accelerates the ions at $A/q \leqslant 8$ to an energy of 6 MeV per nucleon at efficiency not less than 80%.

3. Booster synchrotron, which has a maximum magnetic rigidity of 25 T $\cdot$ m and a circumference of about 215 m. The Booster is equipped with an electron cooling system that allows one to provide cooling of the ion beam in the energy

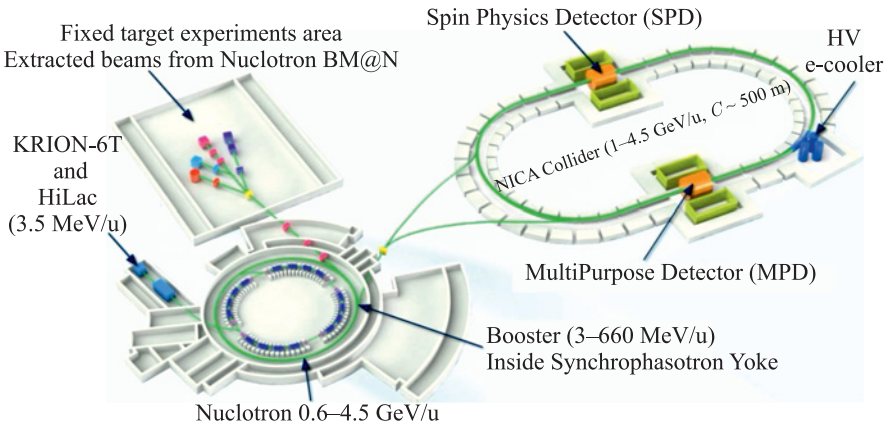

Fig. 2. The NICA accelerator complex at JINR

range from injection energy of up to 100 MeV per nucleon. The maximum energy of Au^{79+} ions accelerated in the Booster is 600 MeV per nucleon. The Booster magnetic system will be manufactured on the basis of the superferric magnets technology.

4. Stripping foil placed in the transfer line from the Booster to the Nuclotron allows one to provide the stripping efficiency at the maximum Booster energy not less than 40%.

5. The Nuclotron accelerator having a maximum magnetic rigidity of 45 T · m and the circumference of 251.52 m provides the ions with the kinetic energy range from 1 to 4.5 GeV per nucleon for Au^{79+}.

6. Two collider rings with a maximum magnetic rigidity of 45 T · m and the circumference of 503.04 m. The maximum field of superconducting dipole magnets is about 4 T. For luminosity preservation an electron or a stochastic cooling system is planned to be constructed. The maximum magnetic rigidity of the collider rings is chosen to be equal to the Nuclotron one in order to have a possibility to increase the center-of-mass energy of heavy-ion collisions up to $\sqrt{s_{NN}} = 11$ GeV.

The NICA collider will have zero beam crossing angle at interaction point and average luminosity of $L = 10^{27}$ cm$^{-2}\cdot$ s^{-1} for gold ion collisions at $\sqrt{s_{NN}} =$ 9 GeV.

The MultiPurpose Detector (MPD) (Fig. 3) is designed to fully exploit the NICA physics potential [7]. The MPD will be a spectrometer with a large uniform acceptance (full azimuth) capable of detecting and identifying hadrons, electrons and gammas at a very high event rate to be achieved at NICA. All the detector elements (see Fig. 3) with overall dimensions of 7×6 m are placed inside a superconducting solenoid generating a homogeneous magnetic field of up to 0.6 T. Tracking will be performed with a cylindrical Time Projection Chamber (TPC) with the MWPC-based readout. The MPD TPC has a high efficiency and momentum resolution over a pseudorapidity range up to $|\eta| < 2$. Having up to 53 measured space points per a track, the TPC will enable particle identification via the ionization energy loss (dE/dx) measurement with a precision better than 8%. At large pseudorapidity the TPC tracking will be supplemented by a multilayer straw tube tracker (ECT) located just after the TPC end plates. The Inner Tracker (IT) consists of four layers of double-sided silicon microstrip detector serving for determination of position of the primary interaction vertex and the secondary decay vertices. The main detector element for hadron identification is the Time-Of-Flight (TOF) system made up of the Resistive Plate Chambers (RPC). The TOF detector covers a pseudorapidity range up to $|\eta| < 3$ and its performance allows one to make a separation of kaons from protons up to the total momentum of 3 GeV/c. Behind the TOF detector, a highly segmented electromagnetic calorimeter (ECAL) for electron and gamma identification will be located. Arrays of quartz counters (FD) are meant for fast timing and triggering, and two

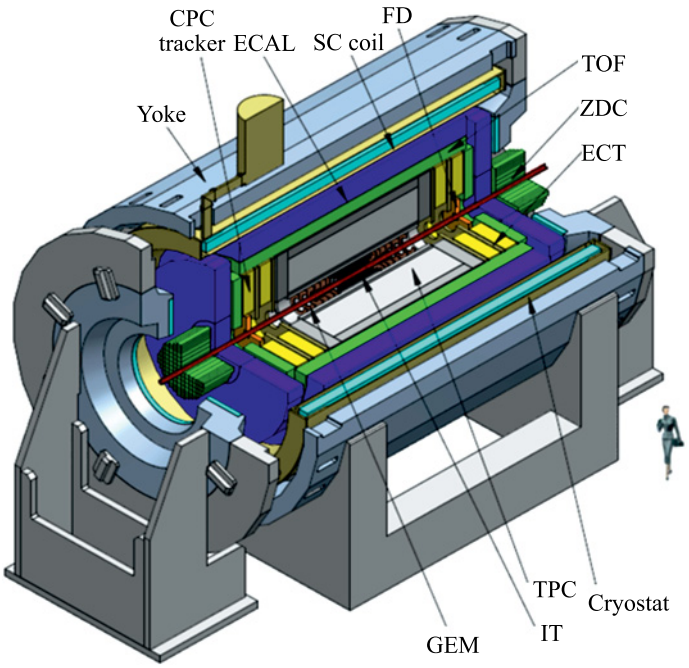

Fig. 3. The MPD detector at NICA

sets of hadron calorimeters (ZDC) covering the rapidity region ($2.5 < |\eta| < 4$) will measure the forward-going energy distribution that is a subject of the offline centrality and event plane analysis.

The MPD detector at NICA will be optimized for a precise study of fluctuations and correlations of the bulk event properties. The primary goal with respect to the above-mentioned consists in measuring of excitation functions and dependence of fluctuations and correlations on centrality and size of colliding nuclei.

Another NICA experiment — the Baryonic Matter at Nuclotron (BM@N) — is a fixed-target experiment at the Nuclotron for study of $A + A$ collisions by measuring a set of observables. The BM@N research program on heavy-ion collisions includes the following topics: investigation of the reaction dynamics and the nuclear EoS, study of the in-medium properties of hadrons, production of (multi)strange hyperons and search for hypernuclei. Particle yields, ratios, transverse momentum spectra, rapidity and angular distributions, as well as fluctuations and correlations, will be studied as a function of the collision energy and centrality. The detector layout is shown in Fig. 4. It combines high-precision track measurements in the GEM and DCH detectors with time-of-flight information for

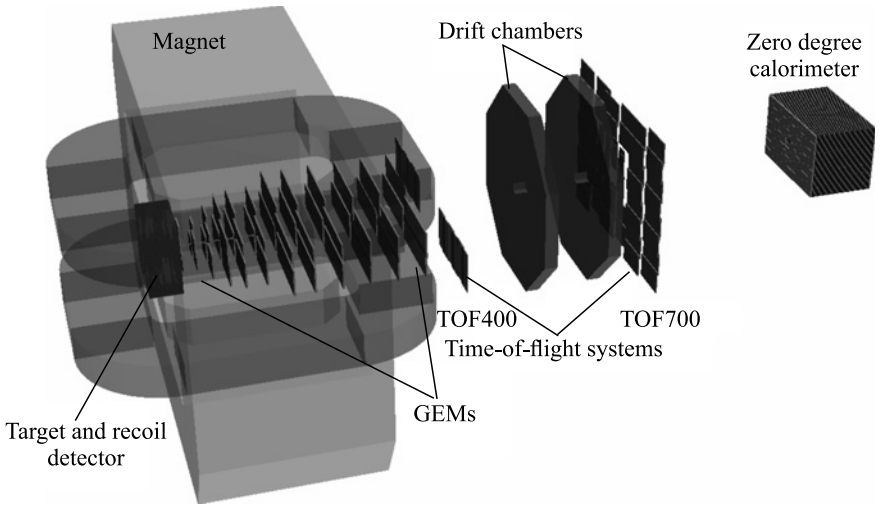

Fig. 4. Layout of the BM@N experiment

particle identification (TOF400 and TOF700) supplemented with the total-energy measurements for the event characterization (ZDC and recoil detector). In order to make a correct interpretation of experimental data obtained from heavy-ion collisions and to provide a normalization for the measured $A + A$ spectra, a detailed study of the elementary reactions $(p + p,\ p + n(d))$ is also planned.

The NICA project realization plan foresees a staged construction and commissioning with the goal to start the BM@N experiment with the Nuclotron extracted beams in 2017. The first technical run of the BM@N detectors was performed with deuteron and carbon beams in spring 2015 aimed to tune the beam line and to test the trigger and data acquisition systems. After modernization of the BM@N beam line elements, xenon ion beam is planned to be used at the end of 2017. At the second stage of the BM@N experiment, at least four planes of two-coordinate silicon strip detectors will be installed between the GEM tracker and the target, and the gold–gold collisions will be studied in 2018. The research program will be continued at higher energies with the MPD setup after putting the startup configuration of the NICA collider into operation in 2019. The commissioning of the design configuration of the NICA accelerator complex is foreseen in 2023.

The paper is structured as follows. In Sec. 1 we present main results on physics simulation for the heavy-ion program at the MPD focusing on collective phenomena, production of hyperons, physics of dileptons and hypernuclei. The main physics objectives of the BM@N experiment are described in Sec. 2. Section 3 is briefly devoted to the NICA White Paper. Section 4 concludes this review with a summary and outline.

1. PHYSICS STUDIES FOR THE MPD

1.1. Collective Phenomena. Collective motion of particles produced in heavy-ion collisions reflects bulk properties of the created matter. Analysis of azimuthal anisotropy resulting from noncentral nuclear collisions appears to be one of the most informative directions in studying the nature and properties of the matter created in high-energy nuclear collisions. The main interest in anisotropic flow is due to its sensitivity to the system properties at the very early stage of fireball evolution. The discovery of large azimuthal anisotropic flow at RHIC provided a conclusive evidence for creation of the dense partonic matter in ultra-relativistic nucleus–nucleus collisions. The state of the newly produced strongly interacting matter is characterized by a very low ratio of shear viscosity to the entropy density η/s, close to a nearly perfect fluid. The origin of anisotropies in the particle momentum distributions lies in the initial asymmetries in geometry of the system. In this way the pressure gradients translate an early spatial asymmetry in density of the initial state to a final-state momentum-space anisotropy. Due to the fact that spatial asymmetries rapidly decrease with time, an anisotropic flow can develop in the very first several fm/c only. In this sense, the anisotropic flow is a unique hadronic observable providing direct information on a stage where the QGP may be one of the main players.

The collective flow is quantified by coefficients in the Fourier series of the particle invariant distribution [8]

$$E\frac{d^3N}{d^3p} \sim 1 + \sum_{n=1}^{\infty} 2v_n \cos\left[n(\phi - \Psi_{\mathrm{RP}})\right],$$

where ϕ is the azimuthal angle of a particle and Ψ_{RP} is the azimuthal angle of the initial-state spatial plane of symmetry (Reaction Plane) defined by direction of the beam and impact parameter vector. By definition, anisotropic flow coefficients look as follows:

$$v_n = \langle \cos\left[n(\phi - \Psi_{\mathrm{RP}})\right] \rangle,$$

where angle brackets denote average over particles and events. Since the impact parameter vector cannot be measured, the anisotropic flow is calculated relative to the so-called *event plane* — a plane of collective expansion of the produced particles. The nth harmonic event plane in an event is defined as

$$\Psi_n = \frac{1}{n} \arctan \frac{\sum w_i \sin n\phi_i}{\sum w_i \cos n\phi_i},$$

where ϕ_i is the azimuthal angle of a particle; w_i is a weighting factor (often set to be equal to value of the transverse momentum p_T or simply 1.0). Thus, the

measured azimuthal flow is defined by a ratio of the *observable flow* to the *event plane resolution*:

$$v_n = \frac{\langle \cos\left[n(\phi - \Psi_n)\right]\rangle}{\langle \cos\left[n(\Psi_n - \Psi_{\mathrm{RP}})\right]\rangle},$$

where denominator is estimated by means of the angular correlation analysis. There exist more sophisticated methods (cumulants, Lee–Yang zeroes) to avoid determination of the reaction plane and to eliminate some nonphysical correlations.

Direct flow v_1 describes sideward motion of nuclear fragments and the newly produced particles. It probes onset of the bulk collective dynamics during thermalization, thus providing valuable information on pre-equilibrium stage. The interest in the direct flow study has recently enhanced considerably due to the recent STAR data on the rapidity dependence $v_1(y)$ obtained from the beam energy scan (BES) program [9]. As demonstrated in Fig. 5, the proton and net-proton slope parameters $dv_1/dy|_{y=0}$ show minimum between $\sqrt{s_{NN}}$ =11.5 and 19.6 GeV.

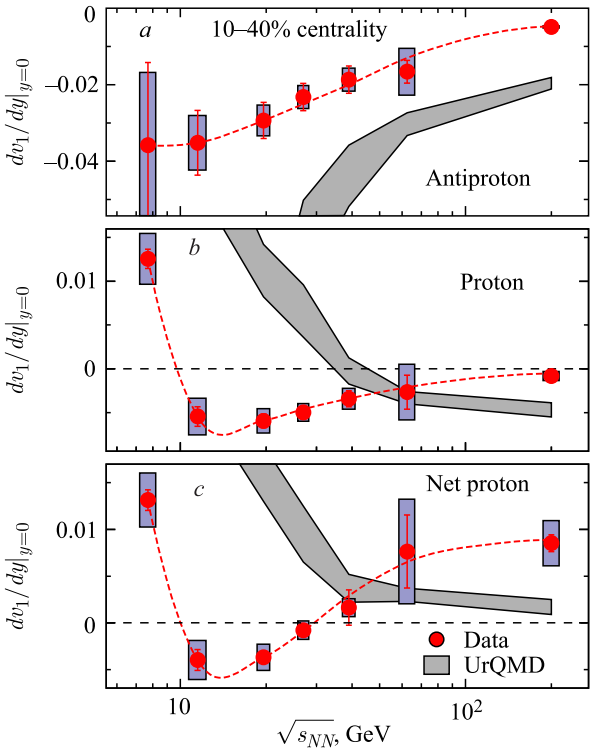

Fig. 5. The direct flow slope (dv_1/dy) near midrapidity versus the center-of-mass energy for midcentral Au + Au collisions as measured by the STAR collaboration [9]

In addition, the net proton $dv_1/dy|_{y=0}$ changes sign twice between $\sqrt{s_{NN}} =$ 7.7 and 39 GeV. The proton and net-proton results qualitatively resemble predictions of a hydrodynamic model with a first-order phase transition from hadronic matter to the deconfined matter. This behavior differs from the hadronic transport calculations [9]. The excitation function of the slope for v_1 was investigated in [10] using the Parton-Hadron-String-Dynamics (PHSD) transport model [11] and the 3-Fluid hydroDynamics (3FD) approach [12]. It was shown that behavior of the slope is sensitive to the nuclear EoS; the best agreement with data was observed for crossover quark–hadron phase transition. The partonic transport model PHSD reproduces a general trend being in a reasonable agreement with the STAR results. NICA has a great opportunity to investigate heavy-ion collisions at the energies where the slope crosses zero line.

The second Fourier coefficient v_2 reflects the azimuthal momentum space anisotropy of particle emission and is known as an elliptic flow. The first attempts

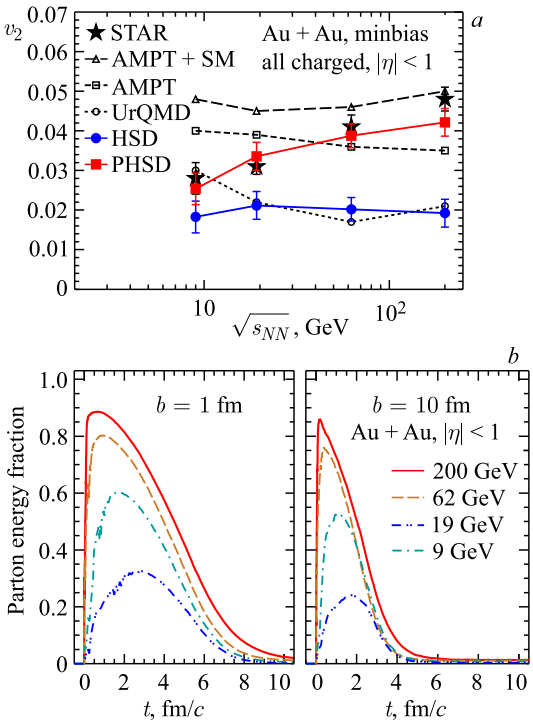

Fig. 6. *a*) The average elliptic flow v_2 of charged particles at mid-pseudorapidity from different models. *b*) Evolution of the parton fraction of the total energy density at midrapidity for different collision energies and impact parameters from the PHSD model. Figures are taken from [13]

to explain the preliminary STAR data with respect to the observed increasing of elliptic flow v_2 with the collision energy have failed since traditional available models did not allow one to clarify role of the partonic phase. In [13] the rise of v_2 was interpreted with the partonic transport model PHSD. In Fig. 6, *a* a complication of experimental data on v_2 is shown along with the results of simulations from several models.

The hadron models (HSD and UrQMD) provide information on contribution from the hadronic phase leading to the fact that flow varies slightly with energy and does not reproduce the available experimental data. The rise of v_2 in the PHSD is traced to a repulsive mean-field potential for partons in the model and partly to higher interaction rates in the partonic medium. The fusion of partons to hadrons or, inversely, the melting of hadrons to partonic quasiparticles occurs when the local energy density is about $\varepsilon \approx 0.5$ GeV/fm^3. The partonic fraction of the energy density at central rapidity is shown in Fig. 6, *b*. It is seen that the partonic phase plays an essential role at high energies. The PHSD model naturally incorporates hadronic and partonic processes. The relative increase of higher flow coefficients v_3 and v_4 in the PHSD is, essentially, due to higher partonic interaction rate and thus to a lower ratio η/s in the partonic medium.

1.1.1. Anisotropic Flow. For this analysis the PHSD model was used as an event generator. The model successfully describes many observables in a wide range of the collision energy [14–19]. Figure 7 demonstrates the calculations for direct v_1 and elliptic v_2 flow for all charged particles from the PHSD model along with the results from the STAR collaboration in the NICA energy range.

The model provides a good description of v_1. Also it describes well v_2 for central and midcentral collisions and a little bit worse for peripheral ones.

Simulations of the MPD detector were performed within the MPDRoot using the "stage 1" geometry. The position of primary vertex was simulated by Monte Carlo according to the expected property of the NICA collider beams ($\sigma_x = \sigma_y = 0.1$ cm, $\sigma_z = 24$ cm). The reaction plane angle was randomly distributed. The charged particles were reconstructed using the Time Projection Chamber (TPC). The event and track selection criteria are summarized in the table. Additionally, we rejected tracks which were identified as electrons with probability more than 60% by energy losses (dE/dx) in the TPC volume.

Using the cuts we selected the primary tracks having a good transverse momentum resolution.

Approximately $0.5 \cdot 10^6$ reconstructed Au + Au events and $1.5 \cdot 10^6$ simulated events were used to perform the analysis.

Event Plane Reconstruction. According to a standard scheme for a track-based detector, the event plane for the elliptic flow can be calculated using the TPC tracks as follows:

$$\Psi_{2,\mathrm{TPC}} = \frac{1}{2} \arctan \frac{\sum w_i \, \sin 2\phi_i}{\sum w_i \, \cos 2\phi_i}.$$

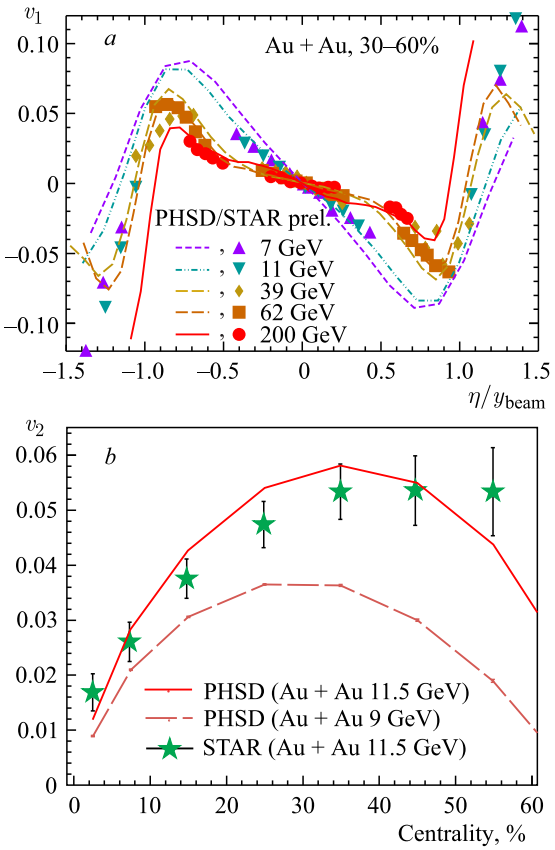

Fig. 7. Direct (*a*) and integrated elliptic (*b*) flow from the PHSD model compared with the STAR results

The cuts used in the analysis

The event selection cuts	
Vertex z position $\lvert v_z \rvert$, cm	< 72
Vertex radius r cut v_r, cm	< 0.43
The track selection cuts	
Pseudorapidity η	< 1.6
Number of hits	> 25
Lower transverse momentum p_T, GeV/c	> 0.15
DCA, cm	< 2

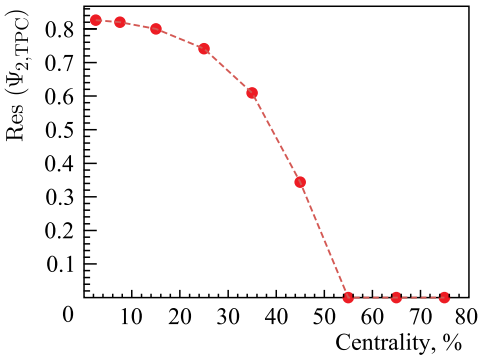

Fig. 8. The event plane resolution for the elliptic flow as defined with the TPC tracks

Resolution for the determined event plane can be estimated by dividing the whole event set into two subsets. Then, the resolution for a subevent is given by

$$\mathrm{Res}\,(\Psi_{2,\mathrm{TPC}}\,\mathrm{sub}) = \\ = \sqrt{\langle\cos\left[2\left(\Psi_{2,a} - \Psi_{2,b}\right)\right]\rangle},$$

where indices a, b denote the corresponding subset. Following [8], the full 2nd event plane resolution was found; the results obtained are shown in Fig. 8.

Due to low multiplicity in peripheral collisions and small value of elliptic flow (see Fig. 7, *b*) the resolution drops very fast. Thus, this method is applicable to central and semicentral collisions only.

Fortunately, the first-order event plane can also be determined from the MPD ZDC detector according to a standard scheme for a hit-based detector:

$$\Psi_{1,\mathrm{ZDC}} = \arctan\frac{\sum \Delta E_i \,\sin\,\phi_i}{\sum \Delta E_i \,\cos\,\phi_i},$$

where the sums run over the energies ΔE_i as measured in the ith calorimeter with angular coordinates

$$\sin\,\phi_i = \frac{y_i}{\sqrt{x_i^2 + y_i^2}}, \qquad \cos\,\phi_i = \frac{x_i}{\sqrt{x_i^2 + y_i^2}},$$

where (x_i, y_i) is a position of the corresponding cell.

The reaction plane in heavy-ion collisions is distributed randomly. However, the rectangular shape of the ZDC leads to a nonuniform distribution of the first-order event plane. Such raw event planes cannot be used in the flow analysis, since they have some preference in their orientations and introduce nonflow correlations. The shift correction can be determined as follows:

$$\Psi' = \Psi + \sum_n^4 \frac{2}{n}\left(-\langle\sin\,n\Psi\rangle\cos\,n\Psi + \langle\cos\,n\Psi\rangle\sin\,n\Psi\right). \qquad (1)$$

The obtained value of the correction for the given analysis, nevertheless, reduces the overall error for the reconstructed flow coefficients.

The event plane resolution correction factor was obtained using a subevent technique. Two "subevents" are defined in every event — in the forward and in the backward η directions. The resolution correction for the event plane measured by each subevent is calculated according to the formula

$$\mathrm{Res}\,(\Psi_{\mathrm{k,ZDC\,sub}}) = \\ = \sqrt{\langle \cos\left[k\left(\Psi_{1,+} - \Psi_{1,-}\right)\right]\rangle}, \quad (2)$$

where $\Psi_{1,+}$ belongs to the calorimeter with $\eta > 0$, and $\Psi_{1,-}$ — with $\eta < 0$. The full event plane resolution for the 1st and the 2nd harmonics (calculated according to [8]) is shown in Fig. 9.

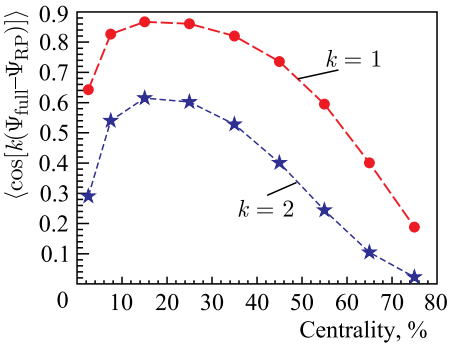

Fig. 9. The event plane resolution for the 1st and the 2nd harmonics from the ZDC information

Since direct flow is opposite in the forward and backward pseudorapidities, the *full* event plane angle can be calculated as follows:

$$\Psi_{1\mathrm{full,\,ZDC}} = \arctan \frac{\left(\sum \Delta E_i \,\sin\,\phi_i\right)_+ - \left(\sum \Delta E_i \,\sin\,\phi_i\right)_-}{\left(\sum \Delta E_i \,\cos\,\phi_i\right)_+ - \left(\sum \Delta E_i \,\cos\,\phi_i\right)_-}, \quad (3)$$

where $(\ )_+$ belongs to $\eta > 0$, while $(\ )_-$ to $\eta < 0$.

Measurements of the event plane angle from the ZDC have some advantages. First of all, a big pseudorapidity gap between two detectors reduces nonflow correlations. Also, it should be emphasized that the reaction plane is determined from the first harmonic flow. This is crucial for several observables.

Direct Flow. Figure 10, *a* shows the reconstructed direct flow as a function of pseudorapidity for charged particles by means of a standard scheme

$$v_1\{\mathrm{EP}\} = \frac{\langle \cos\left[\phi - \Psi_{1\mathrm{full,\,ZDC}}\right]\rangle}{\mathrm{Res}\,(\Psi_{1\mathrm{full,\,ZDC}})},$$

where the event plane angle $\Psi_{1\mathrm{full,\,ZDC}}$ is estimated from the ZDC (3) with the resolution $\mathrm{Res}\,(\Psi_{1\mathrm{full,\,ZDC}})$, which is presented in Fig. 9. The PHSD calculations were done for the fixed reaction plane angle. As can be seen, the reconstructed angle values are in good agreement with the Monte Carlo ones.

The slope of v_1 for the identified (by energy loss in the TPC volume) protons from midcentral collisions is shown in Fig. 10, *b*. Also, predictions from the hadronic (HSD) and partonic (PHSD) models are presented there. The observed difference between the reconstructed slope and the model one appears to be due to efficiency of proton identification.

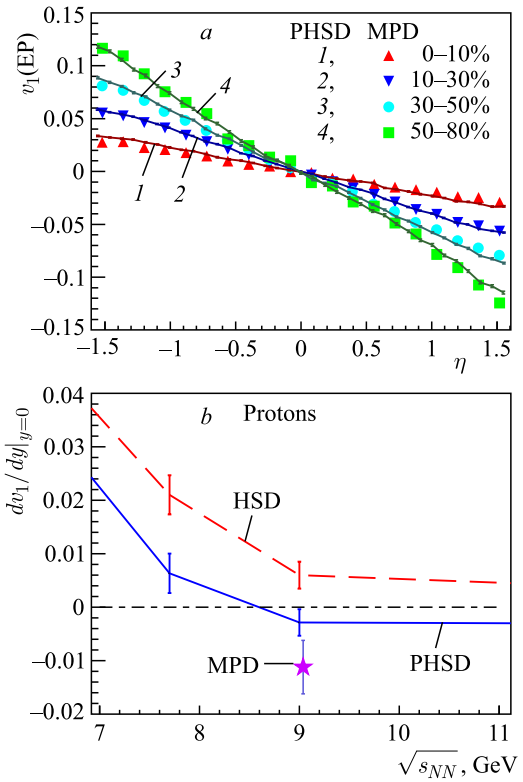

Fig. 10. Direct flow (*a*) for charged particles as a function of pseudorapidity and slope (*b*) of direct flow for protons at midrapidity for Au + Au collisions at $\sqrt{s_{NN}} = 9$ GeV

Elliptic Flow. Each ZDC provides us with the first-order subevent plane, and the flow components can be evaluated according to [20]

$$v_n = \frac{\langle \cos[n(\phi - \Psi_{1,\pm})]\rangle}{\langle \cos[n(\Psi_{1,\pm} - \Psi_{\mathrm{RP}})]\rangle} = \frac{\langle \cos[n(\phi - \Psi_{1,\pm})]\rangle}{\sqrt{\langle \cos[n(\Psi_{1,+} - \Psi_{1,-})]\rangle}} = \\ = \frac{\langle \cos[n\phi]\cos[n\Psi_{1,\pm})] + \sin[n\phi]\sin[n\Psi_{1,\pm})]\rangle}{\sqrt{\langle \cos[n\Psi_{1,+}]\cos[n\Psi_{1,-}] + \sin[n\Psi_{1,+}]\sin[n\Psi_{1,-}]\rangle}}, \quad (4)$$

where $\Psi_{\pm}$ stands for other Ψ_+ or Ψ_-. Since the ZDC has a rectangular shape, one can treat x and y directions separately. Assuming that (4) involves the sine

and cosine terms symmetrically, one can expand it into four terms:

$$
\begin{aligned}
v_{n,+,\cos} &= \frac{2\langle \cos[n\phi]\cos[n\Psi_{1,+}]\rangle}{\sqrt{2\langle \cos[n\Psi_{1,+}]\cos[n\Psi_{1,-}]\rangle}},\\
v_{n,-,\cos} &= \frac{2\langle \cos[n\phi]\cos[n\Psi_{1,-}]\rangle}{\sqrt{2\langle \cos[n\Psi_{1,+}]\cos[n\Psi_{1,-}]\rangle}},\\
v_{n,+,\sin} &= \frac{2\langle \sin[n\phi]\sin[n\Psi_{1,+}]\rangle}{\sqrt{2\langle \sin[n\Psi_{1,+}]\sin[n\Psi_{1,-}]\rangle}},\\
v_{n,-,\sin} &= \frac{2\langle \sin[n\phi]\sin[n\Psi_{1,+}]\rangle}{\sqrt{2\langle \sin[n\Psi_{1,+}]\sin[n\Psi_{1,-}]\rangle}}.
\end{aligned}
\tag{5}
$$

The average over the four terms gives a final result for v_n. Usage of the representation (5) with respect to the standard approach (4) with the full event plane reveals an advantage due to the fact that one can apply corrections to each of the four terms separately according to the detector performance. It gives an opportunity to decrease systematic errors. The reconstructed integrated elliptic flow for all charged particles as a function of centrality is shown in Fig. 11.

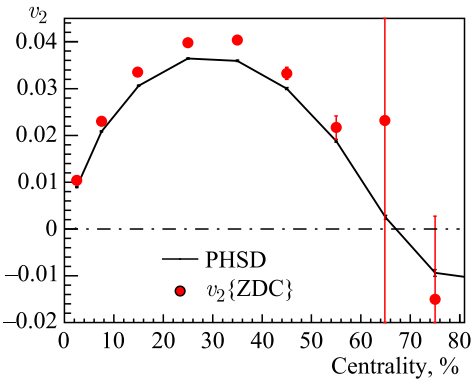

Fig. 11. The integrated elliptic flow $v_2\{\mathrm{ZDC}\}$ as a function of centrality for Au + Au collisions at $\sqrt{s_{NN}} = 9$ GeV

It is extended to all centrality bins and even where the model predicts a negative value of v_2. As was mentioned, peripheral collisions are characterized by a low multiplicity. Along with a small flow observed, it concludes that other methods like $v_2\{\mathrm{EP}\}$ and $v_2\{2\}$ seem to be inapplicable to the analysis.

The differential distributions of v_2 for all charged particles versus pseudorapidity and transverse momentum for several centrality intervals are presented in Figs. 12 and 13, respectively. The reconstructed flow for central and midcentral events reproduces the model distributions, slightly overestimating them.

In the case of peripheral collisions the obtained error bars are essentially big and increasing of the statistics is required. Availability of the end cap detectors is also desirable to enlarge the event plane resolution for the second harmonic.

1.1.2. Charged Azimuthal Correlations. The charge dependence of azimuthal correlations between produced hadrons is an important probe of the QGP matter

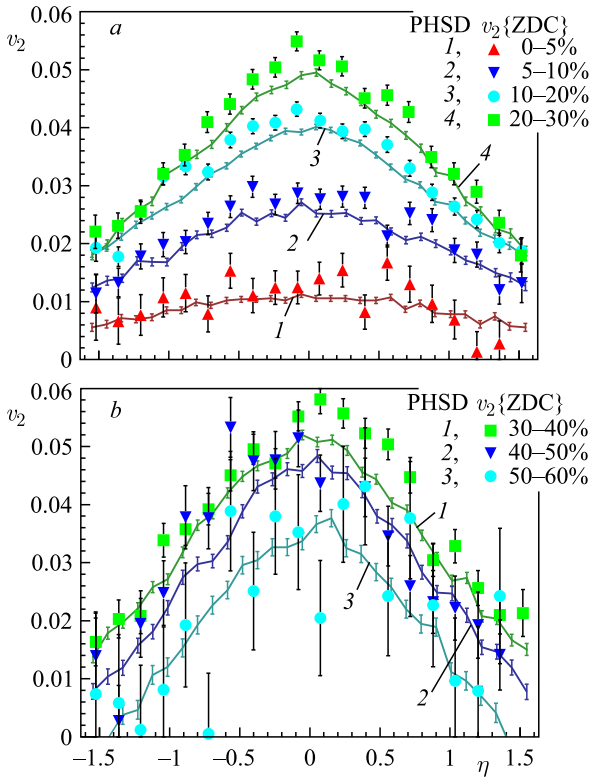

Fig. 12. Elliptic flow $v_2\{\mathrm{ZDC}\}$ as a function of pseudorapidity for several centrality intervals for Au + Au collisions at $\sqrt{s_{NN}} = 9$ GeV

created in relativistic heavy-ion collisions. Recently, it has been argued that the charge-dependent azimuthal correlations can also be sensitive to a possible effect of local parity violation in the QCD [21].

In hot hadronic matter, the topological fluctuations near the critical temperature can create the space-time domains with locally broken P and CP invariances. The local violation of parity can manifest itself in heavy-ion collisions through separation of positive and negative hadrons with respect to the reaction plane; this charge separation would induce an electric dipole moment of the produced hot quark–gluon matter. The charge separation originates from the interplay of a strong magnetic field (and/or the angular momentum) in the early stage of heavy-ion collisions and the presence of topological configurations in hot matter ("the chiral magnetic effect" CME). The recent result from RHIC [22] provides an experimental evidence for this phenomenon in heavy-ion collisions. This effect should be enhanced in the deconfined quark–gluon plasma phase because it

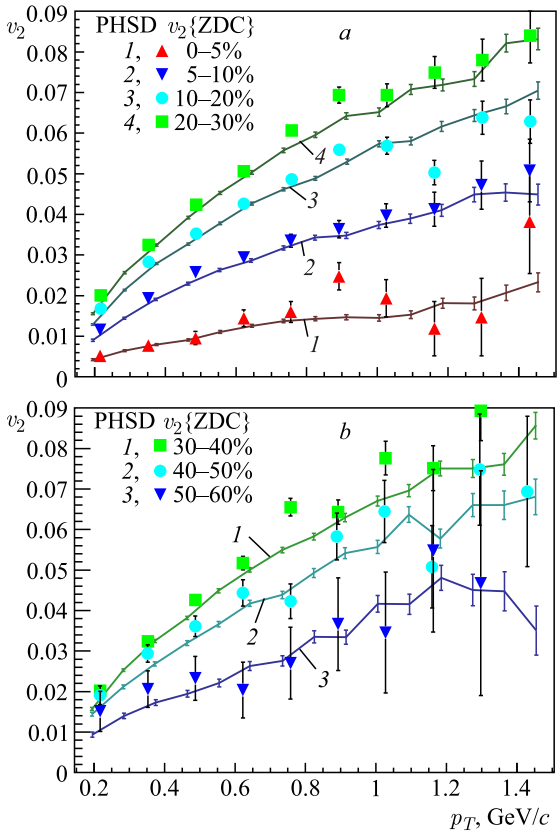

Fig. 13. Elliptic flow $v_2\{\mathrm{ZDC}\}$ as a function of transverse momentum for several centrality intervals for Au + Au collisions at $\sqrt{s_{NN}} = 9$ GeV

requires separation of quarks over a large ("macroscopic" on the scale of hot matter size) distance. There are reasons to expect that the asymmetry will have a peak at some energy, possibly within the energy range of the NICA collider. It should be emphasized that at high baryon density one can also expect a phenomenon of spontaneous parity violation with a number of unique signatures.

In the presence of the strong magnetic field generated in heavy-ion collisions, the local parity violation may result in a separation of charges along the magnetic field which points perpendicular to the reaction plane. Indeed, it was shown that electromagnetic fields of the required strength can be created in relativistic heavy-ion collisions [23–25].

As a signal of possible CP violations in relativistic heavy-ion collisions, it was proposed in [26] to measure the two-particle angular correlation

$\gamma_{ab} = \langle \cos[\phi_a + \phi_b - 2\Psi_{\rm RP}] \rangle$, where $\Psi_{\rm RP}$ is the azimuthal angle of the reaction plane, subscripts a, b represent signs of electric charges being positive or negative and angle brackets denote an average over particles and events. Since the reaction plane is not observable, one has to measure the correlator with respect to the third particle which has to be selected from another rapidity range in order to eliminate a correlation with the primary particle:

$$\gamma_{ab} = \langle \cos[\phi_a + \phi_b - 2\Psi_{\rm RP}] \rangle = \langle \cos[\phi_a + \phi_b - 2\phi_c] \rangle / v_{2,\,c}. \tag{6}$$

The first experimental evidence for the CME, identified via the charge asymmetry, was obtained by the STAR collaboration at RHIC at $\sqrt{s_{NN}} = 200$ and 62 GeV and confirmed qualitatively by the PHENIX collaboration. Recently, these measurements have been extended below the nominal RHIC energy down to $\sqrt{s_{NN}} = 7.7$ GeV within the RHIC BES program (see Fig. 14). In addition, preliminary results for the maximal available energy $\sqrt{s_{NN}} = 2.76$ TeV have recently been announced from the Large Hadron Collider (LHC).

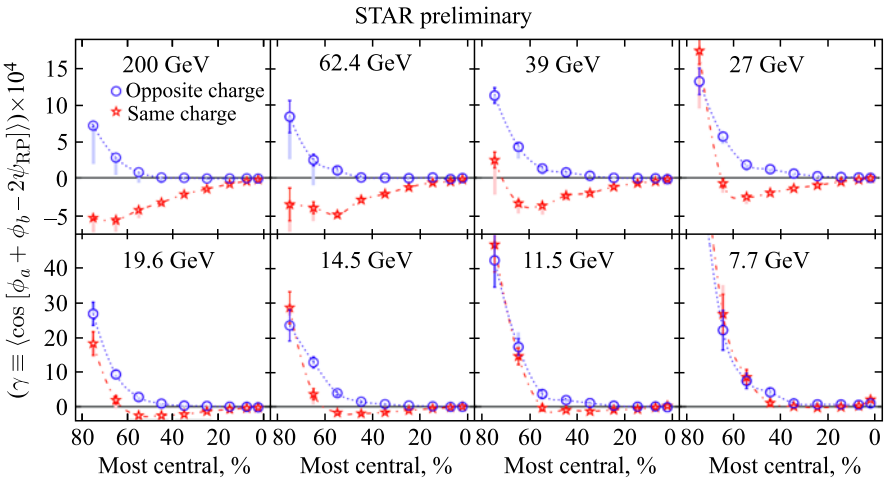

Fig. 14. Azimuthal charged correlations as a function of the collision centrality measured by the STAR collaboration within the beam energy scan program at RHIC [27]

Though at first sight, some features of these data appear to be consistent with expectations from the local parity violation phenomenon, a complete interpretation of the observed effect is still under intense discussion (e.g., [28]).

Background for the CME was investigated in the PHSD model in [25,29,30] with respect to a strong electromagnetic field created in heavy-ion collisions. Thus, the maximal strength of the magnetic field is about $0.13 m_\pi^2$ ($\sim 10^{17}$ G) during the time interval ~ 10 fm/c for Au + Au collisions at $\sqrt{s_{NN}} = 9$ GeV.

Despite such a strong field, within the PHSD model, it was shown that observables are not sensitive to this field in symmetric collisions.

As can be seen from Fig. 15, the pure hadronic HSD model can reasonably describe experimental trends at moderate energies $\sqrt{s_{NN}} = 7.7$ and 11.5 GeV without any CP violation effects.

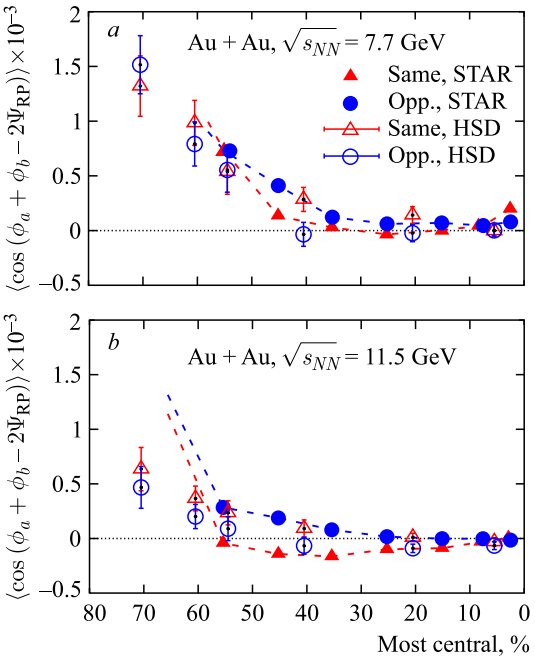

Fig. 15. Azimuthal charged correlations from the HSD model compared to the results of the STAR collaboration. Figures are taken from [29]

An alternative analysis to three-particle correlation (see Eq. (6)) was performed with the event plane reconstructed from energy loss in the ZDC. So, Eq. (6) is transformed to

$$\gamma_{ab} = \langle\cos[\phi_a + \phi_b - 2\Psi_{\mathrm{RP}}]\rangle = \frac{\langle\cos[\phi_a + \phi_b - 2\Psi_1]\rangle}{\langle\cos[2(\Psi_1 - \Psi_{\mathrm{RP}})]\rangle}, \tag{7}$$

where numerator corresponds to the observed value of correlations and denominator is responsible for the event plane resolution. The observed correlations are shown in Fig. 16, *a*. The correlations corrected by the event plane resolution are shown in Fig. 16, *b*. The event plane resolution affects substantially peripheral collisions, where the observed correlations have big error bars and the event plane

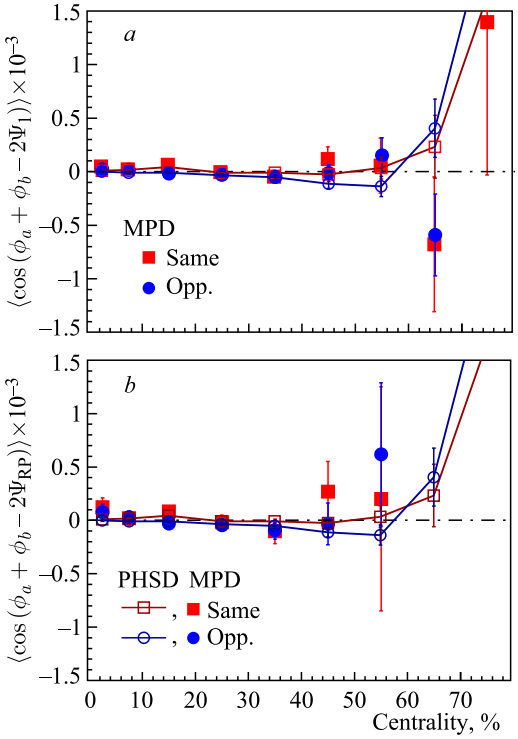

Fig. 16. The observed azimuthal correlations (a) and azimuthal correlations corrected by the event plane resolution (b) as a function of centrality for the same and opposite charged particles for Au + Au collisions at $\sqrt{s_{NN}} = 9$ GeV

resolution is low. The magnitude of γ_{ab} is very small and requires much more statistics or more precise determination of the event plane.

It is of further interest to consider the average $\langle \cos [\phi_a - \phi_b] \rangle$ that is supposed to be independent of the reaction plane and can be used in order to estimate systematic errors. As can be seen from Fig. 17, peripheral collisions incorporate some errors.

Following [28], one can expand the correlations (7) into *in-plane* and *out-of-plane* components as follows:

$$\begin{aligned} \langle \cos [\phi_a + \phi_b - 2\Psi_{\mathrm{RP}}] \rangle = \langle \cos [\phi_a - \Psi_{\mathrm{RP}}] \cos [\phi_a - \Psi_{\mathrm{RP}}] \rangle + \\ + \langle \sin [\phi_a - \Psi_{\mathrm{RP}}] \sin [\phi_a - \Psi_{\mathrm{RP}}] \rangle, \\ \langle \cos [\phi_a - \phi_b] \rangle = \langle \cos [\phi_a - \Psi_{\mathrm{RP}}] \cos [\phi_a - \Psi_{\mathrm{RP}}] \rangle - \\ - \langle \sin [\phi_a - \Psi_{\mathrm{RP}}] \sin [\phi_a - \Psi_{\mathrm{RP}}] \rangle, \end{aligned}$$

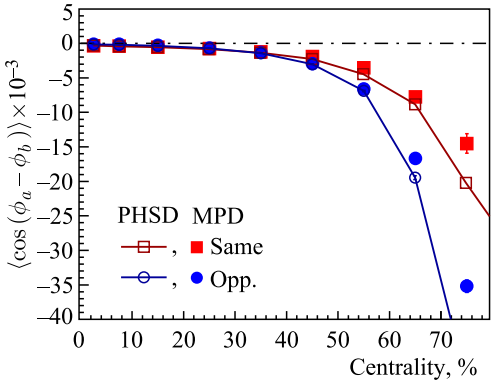

Fig. 17. Azimuthal correlations as a function of centrality for Au + Au collisions at $\sqrt{s_{NN}} = 9$ GeV

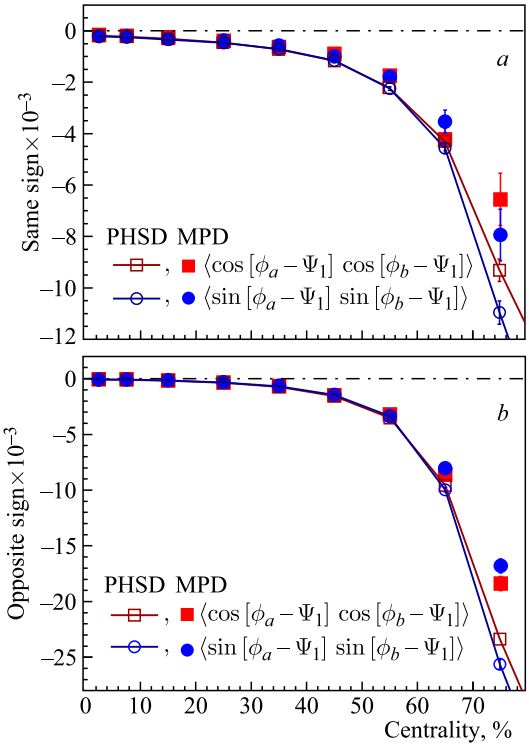

Fig. 18. The observed projections of azimuthal correlations on the *in*- and *out-of*-reaction plane directions for the same (*a*) and opposite (*b*) charged particles from Au + Au collisions at $\sqrt{s_{NN}} = 9$ GeV

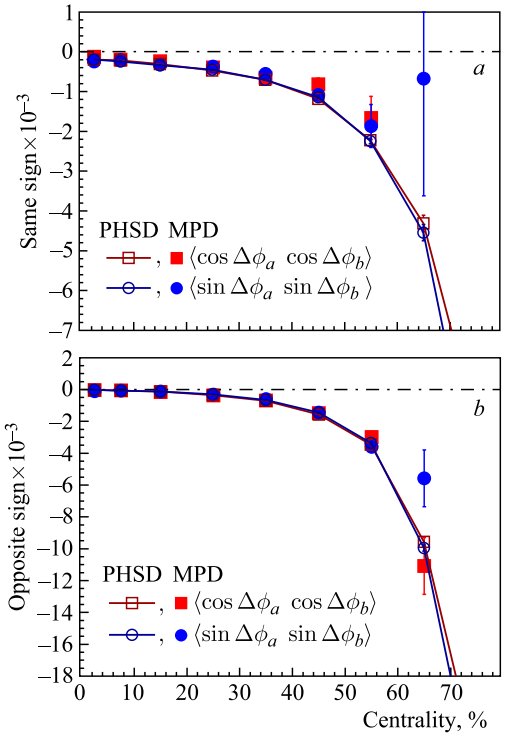

Fig. 19. The observed projections of azimuthal correlations on the *in*- and *out-of*-reaction plane direction for the same (*a*) and opposite (*b*) charged particles from Au + Au collisions at $\sqrt{s_{NN}} = 9$ GeV corrected by the event plane resolution

where *sine* term corresponds to *out-of-plane* correlations, *cosine* — to *in-plane* ones. The observed projections for the same (plot *a*) and opposite (plot *b*) charged particles are presented in Fig. 18, the corrected ones — in Fig. 19.

The azimuthal correlations and their projections are well reconstructed for central and midcentral collisions. In the case of peripheral collisions one has to increase statistics or determine the event plane more accurately combining the ZDC with the end-cap detectors.

1.1.3. Baryon Stopping Power. Baryon stopping power is a requisite in describing the conversion of the initial particle collision energy into the matter excitation and creation of hot and dense nuclear matter. The issue of the baryon stopping power in heavy-ion collisions has been studied from SIS to the LHC energies. A direct measure of the baryon stopping is the net-baryon rapidity distribution. However, since experimental information on neutrons is usually unavailable, net-proton (i.e., proton-minus-antiproton) data are used in the analysis.

In [31] it was argued that the baryon stopping in nuclear collisions can be a sensitive probe for the onset of deconfinement.

The statistical-thermal model is now a well-established one in the analysis of relativistic heavy-ion collisions, and it allows one to study dependence of the chemical freeze-out temperature T on the baryonic chemical potential μ_B. The freeze-out curve in the $T-\mu_B$ plane can also be drawn in the energy density vs. the net-baryon density plane as shown in Fig. 20. The figure shows that the highest net-baryon density will be reached in the beam energy range covered by the NICA accelerator. So, an influence of the baryon density on the particles properties will be clearly seen at the NICA energies.

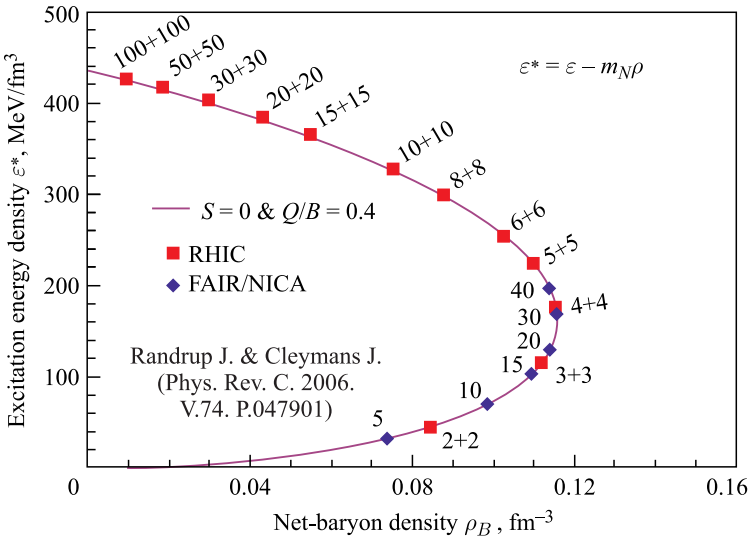

Fig. 20. The hadronic freeze-out line in the $\rho_B - \varepsilon^*$ phase plane as obtained from the values of μ_B and T that have been extracted from the experimental data [32]. The beam energies (in GeV/nucleon) for which the particular freeze-out conditions expected at either RHIC or FAIR or NICA are also indicated

Available data on the proton (at the AGS energies) and net-proton (at the SPS energies) rapidity distributions from central heavy-ion collisions in the midrapidity region are presented in Fig. 21. The data at $10A$ GeV are repeated in Fig. 21, *b* in order to keep the reference spectrum shape for comparison. The data are plotted as functions of a "dimensionless" rapidity $(y-y_{\rm cm})/y_{\rm cm}$, where $y_{\rm cm}$ is the center-of-mass rapidity of colliding nuclei. In particular, this is a reason why the experimental distributions are multiplied by $y_{\rm cm}$. This representation is chosen in order to make different distributions of approximately the same width and the same height. This is convenient for comparison of shapes of these distributions. To

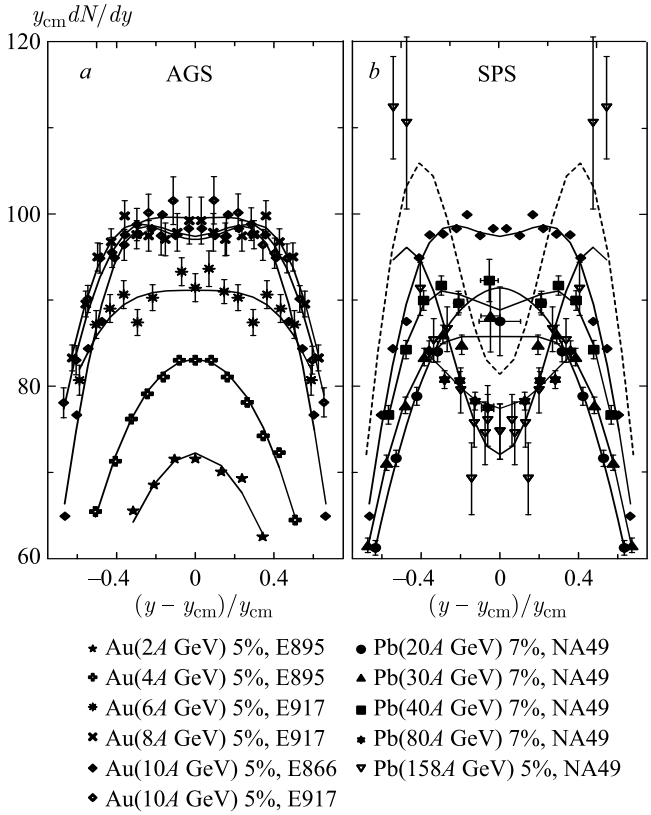

Fig. 21. Rapidity spectra of protons (for the AGS energies) and net protons $(p - \bar{p})$ (for the SPS energies) from central collisions of Au + Au (AGS) and Pb + Pb (SPS). The plot is taken from [1, p. 131]. The percentage shows fraction of the total reaction cross section, corresponding to the experimental selection of central events. The solid lines connecting points represent the two-source fits by (8). The dashed line is the fit to old data on Pb($158A$ GeV)+ Pb [33], these data themselves are not displayed

make this comparison more quantitative, the data are fitted by the simple formula

$$\frac{dN}{dy} = a\left(\exp\left\{-(1/w_s)\cosh\left(y - y_s\right)\right\} + \exp\left\{-(1/w_s)\cosh\left(y + y_s\right)\right\}\right), \quad (8)$$

where a, y_s and w_s are parameters of the fit.

As shown in Fig. 21, the experimentally observed baryon stopping indicates (within the present experimental uncertainties) a nonmonotonous behavior as a function of incident energy of colliding nuclei. This reveals itself in a "wiggle" irregularity in the excitation function of the midrapidity reduced curvature C_y (9) of the (net-)proton rapidity spectrum (see Fig. 22).

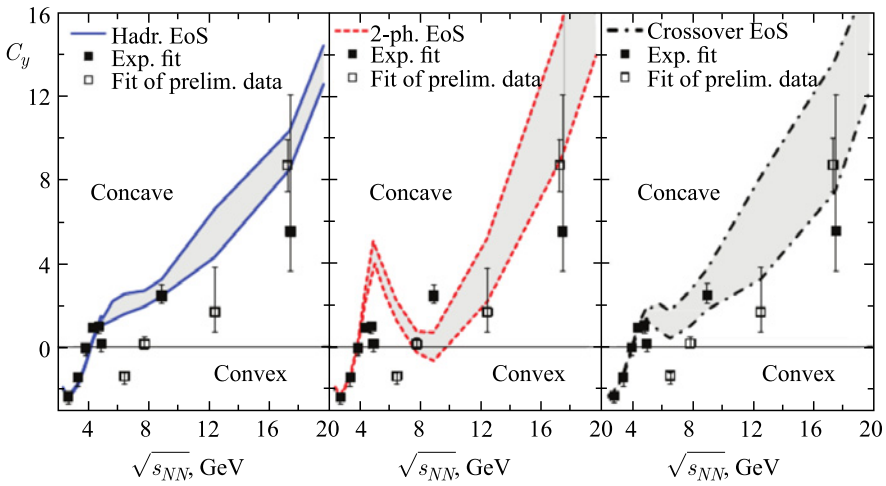

Fig. 22. Midrapidity reduced curvature of the net-proton rapidity spectrum as a function of the incident center-of-mass energy of colliding nuclei as deduced from the experimental data and predicted by the 3FD calculations with different EoSs. Upper borders of the shaded areas correspond to the fits confined in the region of $|y - y_{\rm cm}|/y_{\rm cm} < 0.7$, lower borders — in $|y - y_{\rm cm}|/y_{\rm cm} < 0.5$

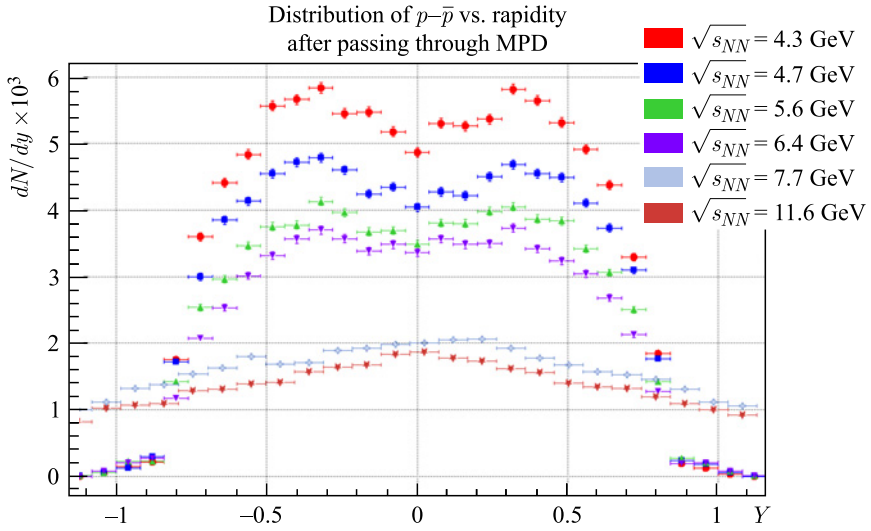

Fig. 23. Dependence of the net-proton distribution on rapidity for Au + Au collisions at the NICA energy scan

The "wiggle" behavior is reproduced qualitatively by the 3-fluid dynamics model (3FD) [12] calculation with the EoS involving a first-order phase transition into the quark–gluon phase, while with the hadronic EoS it fails to reproduce this irregularity [34]:

$$C_y = \left(y_{\rm beam}^3 \frac{d^3N}{dy^3}\right)_{y=0} \Big/ \left(y_{\rm beam}\frac{dN}{dy}\right)_{y=0} = \\ = \left(\frac{y_{\rm beam}}{w_s}\right)^2 \left(\sinh^2 y_s - w_s \cosh\, y_s\right). \quad (9)$$

To estimate this effect at the NICA energies, we use the 3FD model with particlization procedure used for the UrQMD3.4 model [35]. The result of this simulation shown in Fig. 23 clearly indicates such peak-deep-peak behavior at midrapidity even with the simulation response for the MPD detector.

1.1.4. Femtoscopic Studies at the NICA Energies. Size and temporal parameters of the particle-emitting region at freeze-out can be extracted by use of femtoscopic techniques. Momentum correlations of two particles at small relative momenta in their center-of-mass system (CMS) are widely used for studying space-time characteristics of heavy-ion collisions at a level of $= 10^{-15}$ m, giving a correlation femtoscopy tool [36–42]. The femtoscopic correlations due to quantum statistics (QS) of the produced identical particles were observed more than 50 years ago as an enhanced production of pairs of identical pions with small opening angles (GGLP effect). A general base of the modern correlation femtoscopy was proposed by G. I. Kopylov and M. I. Podgoretsky (JINR, Dubna) in the early 70s of the previous century. Moreover, the effect of particle final state interaction (FSI) allows one to extend correlation femtoscopy also to nonidentical particles [43]. Along with the space-time characteristics, the FSI effect provides valuable information also on low-energy strong interaction between any abundantly produced particles, which can often be hardly achieved by other techniques.

The performed experiments at RHIC clearly demonstrate that hot and dense matter with the partonic collectivity is formed in the ultrarelativistic heavy-ion collisions at large $\sqrt{s_{NN}}$ [2, 3, 5, 44]. The observed effects (jet quenching, charmonium suppression, strangeness enhancement, etc.) are considered to be the signals of a transition to the deconfined phase. It should be stressed that information on the space-time evolution of hot and dense matter under extreme conditions in heavy-ion collisions can be extracted by study of the femtoscopy correlations only.

Taking into account the on-mass-shell constraint, $q_0 = \mathbf{vq}$, the correlation function at a given pair 3-velocity $\mathbf{v}$ can be expressed as a function of the so-called out, side and longitudinal components of the relative 3-momentum $\mathbf{q}$ [44]; the out and side denote the transverse components of the vector $\mathbf{q}$, the out

direction is parallel to the transverse component of the pair 3-velocity. The correlation function is usually parameterized in terms of the Gaussian correlation (femtoscopic) radii R_i, e.g., for spin-0 non-interacting bosons:

$$C(q_{\rm out}, q_{\rm side}, q_{\rm long}) = \\ = 1 + \lambda \exp\left(-R^2_{\rm out} q^2_{\rm out} - R^2_{\rm side} q^2_{\rm side} - R^2_{\rm long} q^2_{\rm long} - 2R^2_{\rm out,long} q_{\rm out} q_{\rm long}\right), \quad (10)$$

and the radii dependence on pair rapidity and transverse momentum is studied. The correlation strength parameter λ can differ from unity due to contribution of long-lived emitters, particle misidentification and coherence effects. Equation (10) assumes azimuthal symmetry of the production process [44]. Generally, e.g., in case of the correlation analysis with respect to reaction plane, one should account for all the three cross terms $q_i q_j$.

It is well known that particle correlations at high energies usually measure only a small part of the space-time emission volume, the correlated particles with nearby velocities being emitted by almost comoving sources and so — at nearby space-time points. To eliminate the effect of the longitudinal motion, the correlations can be analyzed in terms of the invariant variable $Q = (-q^2)^{1/2} = 2k^*$ and the components of the momentum difference in the PRF, or in the longitudinally comoving system (LCMS) [45], in which each pair is emitted transversely to the reaction axis. In the midrapidity region one can exploit the longitudinal boost invariance, leading to the independence of the correlation function in the LCMS or PRF from pair rapidity and vanishing cross term in (10). In the following, we will assume the correlation radii determined in the LCMS and exploit the reduction of the 6D correlation functions to the 4D ones (in case of the azimuthally symmetric analysis), depending on the three components of the relative momentum and the magnitude of the pair transverse momentum only.

Study of femtoscopic correlations allows one to constrain the model predictions for an early stage of collision and fireball evolution. It was expected that the first-order phase transition strongly delays the fireball evolution [46], but the pion correlation radii measured in a wide energy range (from the AGS to the RHIC energies) demonstrated a weak energy dependence (see Fig. 24) and did not reveal the expected behavior for the phase transition [47–56]. The weak energy dependence of femtoscopic radii in the AGS–SPS–RHIC energy region and the overestimation of these radii by various transport and hydrodynamic models was considered as a femtoscopy puzzle.

This puzzle motivated a development of more sophisticated hydrodynamic models allowing for a simultaneous description of single particle and correlation observables, including the femtoscopic ones. According to them, the femtoscopic radii, particle spectra and elliptic flow can be described using the initial Gaussian density profile [57] and by including a combination of several effects: prethermal acceleration, a stiffer EoS and adding viscous corrections [58].

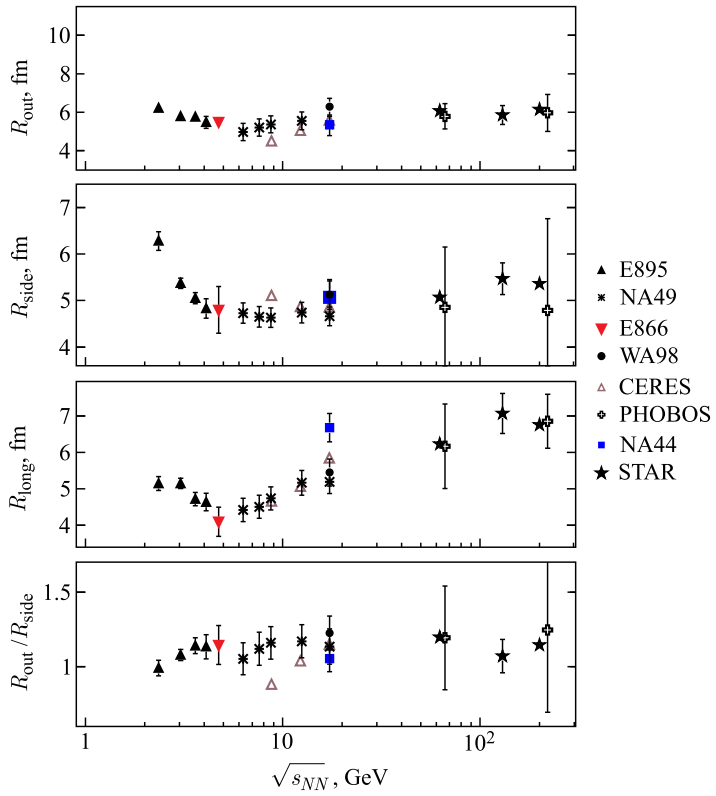

Fig. 24. Energy dependence of correlation radii for different experiments

The heavy-ion collisions at the highest RHIC energies are described assuming a crossover transition at high temperature T and vanishing baryonic chemical potential μ_B. At the same time, there are models that predict a strong first-order phase transition at moderate temperatures and large μ_B [59], which takes place at moderate and low energies. Therefore, the NICA complex operating in the energy region $\sqrt{s_{NN}} = 4{-}11$ GeV is suitable for the critical-point location search via experimental detection of its signatures.

According to various theories, the main signatures of the critical point are:

1) nonmonotonic behavior of some observables;

2) increasing of fluctuations occurring near the critical point;

3) nonequilibrating final state expected after cooling through a first-order phase transition, leading to the non-Gaussian fluctuations.

The indications of something unusual at lower energies came from the NA49 at SPS, where a “horn” at $\sqrt{s_{NN}}$ = 7 GeV was observed. Therefore, a question

on the partonic properties change or their "turn off" is arising. The low energy scan planned to be performed at the NICA complex could shed light on evolution of the unusual medium properties with beam energy.

The predicted increase of emission time due to a phase transition of the first order should be reflected in increasing of $R_{\rm out}/R_{\rm side}$ ratio, but it was observed neither at the high RHIC energies, nor at the low AGS–SPS energies.

Possible reasons why it was not observed at low energies could be the following [60]:

1) decrease of relative contribution of the QGP phase at low energies;

2) contribution of small-size sources dominates as leading to a wider correlation effect.

These issues indicate that more complicated techniques beyond the usual 3D Gaussian parameterizations are necessary to extract the relevant information on space-time characteristics of the produced QGP matter. Also the correlation analysis with respect to the reaction plane [39] and spherical harmonic expansion [61], which can be used only in case of the huge available statistics, is considered to be useful in this context.

A large luminosity planned at NICA, together with a set of precise large acceptance detectors, will give an opportunity for a more sophisticated study of a great many combinations of identical and nonidentical particles, thus providing much more detailed space-time information on the emitting system than in the previous studies.

The final-state interactions (FSI) between pairs of nonidentical particles provide information on the average relative space-time shift between emission points of two particle species in the PRF [62]. Obviously, such information is unavailable from correlations of identical particles, which allow one to access only the even moments of the separation distribution. Note that the spatial shifts in PRF are particularly sensitive to time delays in particle production and to collective flow — the heavier particles being shifted more to the expanding fireball edge than the lighter ones. This technique thus yields quite valuable information about the production dynamics of various particle species. For example, it allows one to check the expected earlier freeze-out of multistrange baryons as compared with pions.

Experimentally, in case of identical particles at small relative momenta effects like a hit sharing, track overlapping and track splitting must be considered very precisely within the femtoscopic analysis. To do it, many detailed simulations aimed to eliminate influence of systematic distortions are obligatory. The track splitting can lead to an enhancement of pairs at low relative momentum. The enhancement arises when a single track was reconstructed as two with very similar momenta. The track merging reveals itself when two particles are reconstructed as one track. The merged tracks decrease the number of pairs at low relative momentum due to the fact that particles having a higher probability to be merged

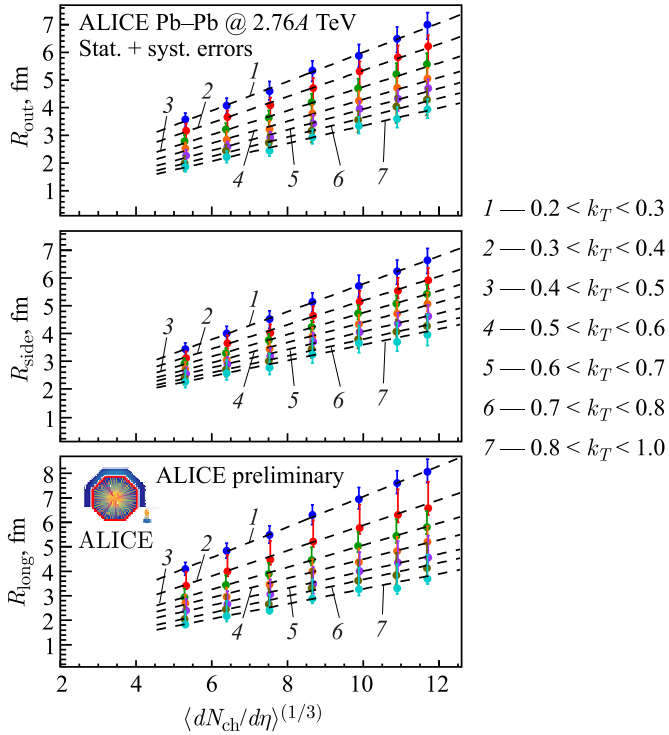

Fig. 25a. Femtoscopic radii for Pb–Pb collisions as a function of event multiplicity, for different ranges of pair momentum k_T. The top, middle, and bottom panels show $R_{\rm out}$, $R_{\rm side}$ and $R_{\rm long}$, respectively. The error bars correspond to the combined statistical and systematic uncertainties

are those with similar momenta. To eliminate the effect, it is required that all pairs entering the numerator and denominator of correlation function should have a fraction of the merged hits of no more than 10% [58].

It is known from [42] that the three-dimensional femtoscopic radii measured in many experiments over a wide range of energies scale linearly with cube root of the measured charged particle multiplicity. An example of such behavior obtained by the ALICE collaboration [63] is presented in Fig. 25a.

In order to check whether the effect observed in [42] is seen at the NICA energies, we performed a simulation of 1 million Au + Au collisions at $\sqrt{s_{NN}}$ = 11 GeV using the UrQMD model and taking into account hydro evolution of the colliding system. At the performed simulation, a transition of crossover type was chosen as the EoS used. The track cuts used correspond to the ALICE acceptance ($0.15 \leqslant p_T \leqslant 1$ GeV/c, $|\eta| \leqslant 1$).

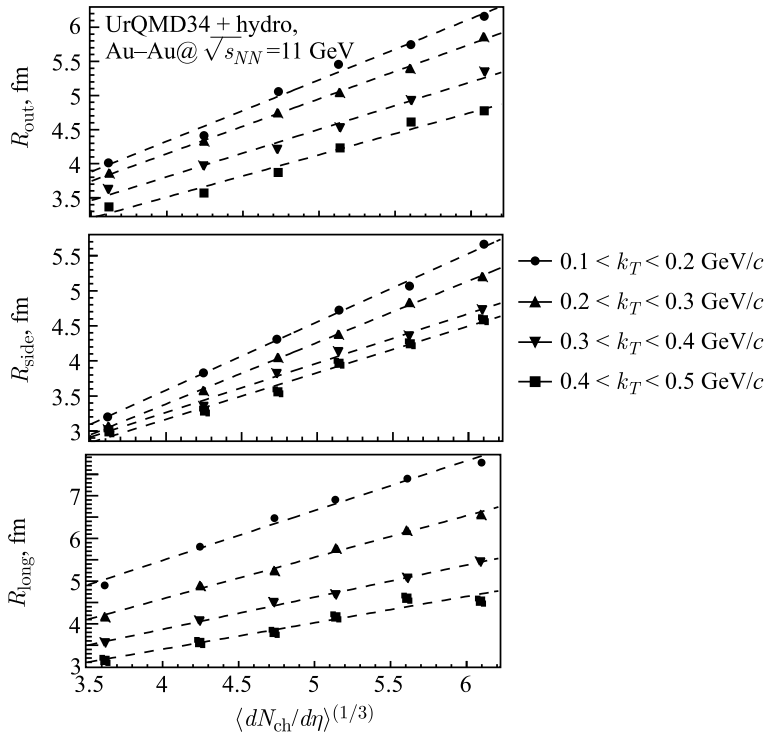

Fig. 25b. Femtoscopic radii for Au–Au collisions as a function of event multiplicity, for different ranges of pair momentum k_T. The top, middle, and bottom panels show $R_{\rm out}$, $R_{\rm side}$ and $R_{\rm long}$, respectively. The transverse momenta of pairs with $k_T > 0.6$ GeV/c are not presented due to lack of the available statistics

The LCMS Gaussian radii fitted according to (10) with the omitted cross term are presented in Fig. 25b. The observed approximate linear scaling of the three-dimensional radii looks similar to those seen by the ALICE collaboration except for different slopes. In fact, the universal slopes settle only at top RHIC energies in correspondence with the dominantly partonic nature of the produced fireball and its universal freeze-out density at these and higher energies. In such a case it will be interesting to study the multiplicity dependence of the femtoscopic radii in the transition region at the NICA energies experimentally.

The next point to be considered is related to the freeze-out time ($t_{\rm fr}$) of the interacting system depending on the used EoS. The analysis was performed also using the UrQMD model (the hydro stage of evolution is included). The obtained results are presented in Fig. 26.

It is possible to conclude that the hydro stage lasts longer in case of the first-order phase transition.

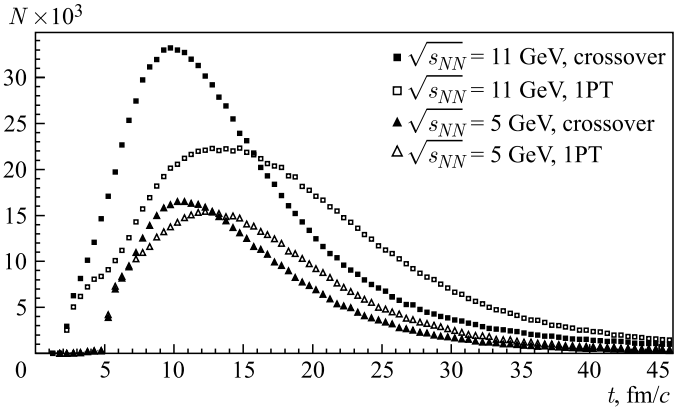

Fig. 26. Distribution over $t_{\rm fr}$ depending on $\sqrt{s_{NN}}$ and the used EoS. 1PT corresponds to the EoS assuming the first-order phase transition

To obtain more detailed information on the space-time structure of the system, as compared with that in Gaussian correlation radii, one can use more complicated parameterizations accounting for non-Gaussian tails, or exploit the source imaging technique [64, 65]. The latter is based on Fourier-like extraction of the emission function from the measured correlation function in the PRF; being formally model-independent, it is however quite unstable thus requiring still some stabilizing model assumptions. In principle, these techniques allow one to reveal the effect of delayed emission due to the onset of the first-order phase transition, as well as other effects leading to a complex form of the source function, such as collective flows, resonances or rescatterings.

In Fig. 27, projections of the source function in the PRF on out, side and longitudinal directions are presented. The source function was obtained for pions at different $\sqrt{s_{NN}}$ using the UrQMD model. It was established that the source function is not very sensitive to k_T and, due to this fact, the pion pairs used in the analysis satisfy the condition $0.2 \leqslant k_T \leqslant 0.4$ GeV/c. Also, there was applied a cut on pseudorapidity ($|\eta| < 0.5$). One may see that for calculations with the first-order phase transition the visible tails of the source function are longer than those obtained using crossover. The largest difference is seen in the longitudinal direction, the effect becoming more visible with the increasing energy.

1.2. Measurements of Dilepton Spectra at NICA/MPD. The correlated e^+e^- pairs ($dileptons$) are particularly useful probes to study dense nuclear matter formed in heavy-ion interactions. As predicted by the QCD-inspired models, the key properties of hadrons are modified in the medium of the density and temperature regimes encountered in heavy-ion reactions. In contrast to the vacuum situation, a hadron cannot only decay in a hot and dense medium but also in-

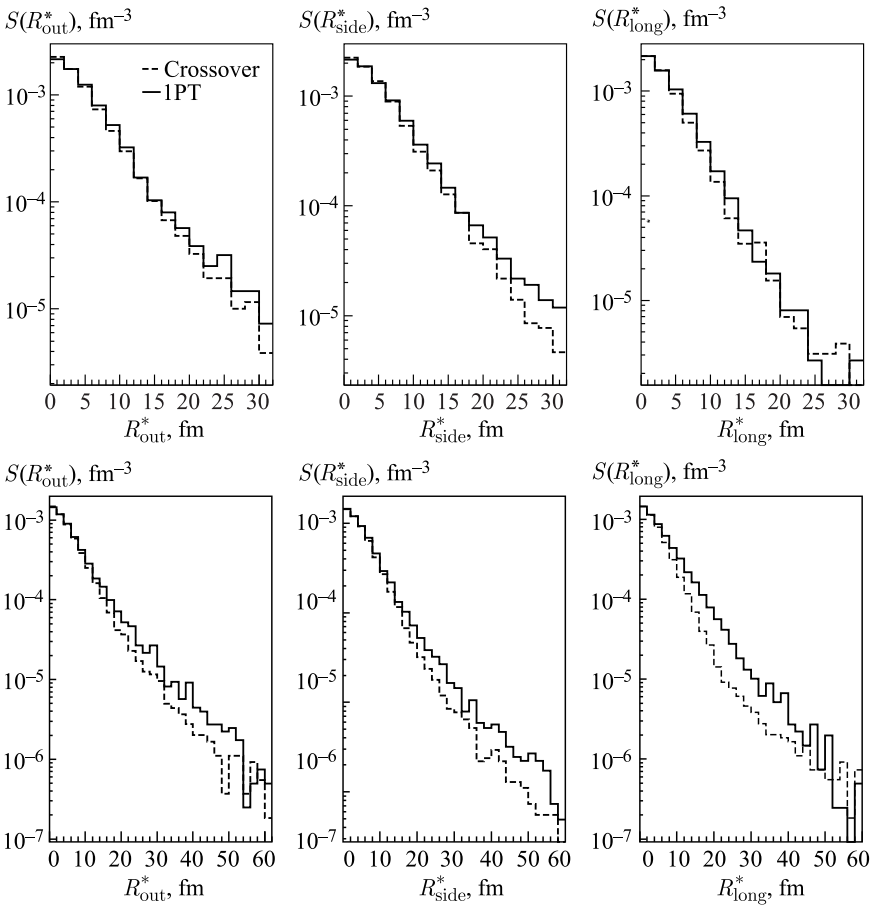

Fig. 27. Projections of the source function in the PRF obtained for pions at $\sqrt{s_{NN}} = 5$ GeV (top row) and $\sqrt{s_{NN}} = 11$ GeV (bottom row) within the UrQMD model. 1PT, represented by the solid line, corresponds to the EoS with the first-order phase transition

teract with the constituents in scattering processes and resonance excitation. The generic outcome of these interactions is an appreciable broadening of the spectral peaks with a possible mass shift [66–68]. Such modifications of hadron properties may be associated with a decrease in the chiral condensate with increasing density and temperature, leading to partial restoration of chiral symmetry which is spontaneously broken in the vacuum due to nonvanishing quark masses. Medium modifications may be reflected in the invariant mass distribution of the electron–positron pairs as an enhanced production of dileptons above known sources in nucleus–nucleus collisions. The experimental evidence for such an enhancement

was provided at the SPS energies by the CERES and NA60 collaborations. Despite the obvious progress made in this field and a number of experiments that measured dilepton continuum, the many questions have not been answered yet and require new high precision experimental data to clarify the situation. For example, until now, no dilepton measurements have been performed at the center-of-mass energies of several GeV and the NICA–MPD dilepton program is aimed to fill this gap. The range of collision energies $4 < \sqrt{s} < 11A$ GeV is very promising for such measurement since the effect of modifications is expected to be sensitive to the baryon density, while the latter happens to reach the maximum in central Au + Au collisions at NICA [69] (see Fig. 20).

Advantages of studying vector mesons (ρ, ω, ϕ) via their decays to lepton pairs are: 1) vector mesons have very short lifetimes as compared to that of the fireball; 2) the decay products of vector mesons (namely, e^+, e^-, μ^+, μ^-) interact only electromagnetically and escape the interaction region unaffected by subsequent strong interactions, thus carrying to the detectors information about the conditions and properties of the medium at the time of their creation. However, experimental study of dileptons in heavy-ion collisions is a challenging task, because of a huge combinatorial background of uncorrelated lepton pairs from the Dalitz decays of η and γ conversions. The second difficulty is the physics background. Dileptons can be emitted by a variety of sources and, therefore, before claiming observation of any new effect, it is mandatory to have a thorough understanding of the expected contribution from all the known sources.

The MPD performance for study of dileptons was investigated with a dedicated Monte Carlo simulation task. The study was aimed at determination of the hadron suppression factor of the MPD particle ID system, signal-to-background ratio and invariant mass resolution in the region of masses of vector mesons. A detailed description of the analysis procedure and results can be found in [70]. Central Au–Au collisions from the UrQMD generator were combined with the cocktail of vector mesons from the Pluto event generator. All the particles from the events were transported through the detector setup (see Fig. 3) which includes the Time Projection Chamber (TPC), Time-Of-Flight system (TOF) and Electromagnetic Calorimeter (EMC) (covering $|\eta| < 1.2$) with the Geant code. A realistic detector response was simulated followed by tracking, TPC–TOF matching and particle ID tasks which were performed within the MPDRoot framework. Typical efficiency of track matching with the TOF was found to be better than 90% at transverse momentum greater than 0.4 GeV/c, and the transverse momentum resolution appeared to be better than 3% for $p_T < 1$ GeV/c. Electron identification was achieved by using combined information about the specific energy loss dE/dx from the TPC, time-of-flight from the TOF and E/p from the EMC. After applying the PID cuts, the achieved overall hadron rejection factor was about 3200. The background from conversion pairs was eliminated by a set of topological and kinematical cuts.

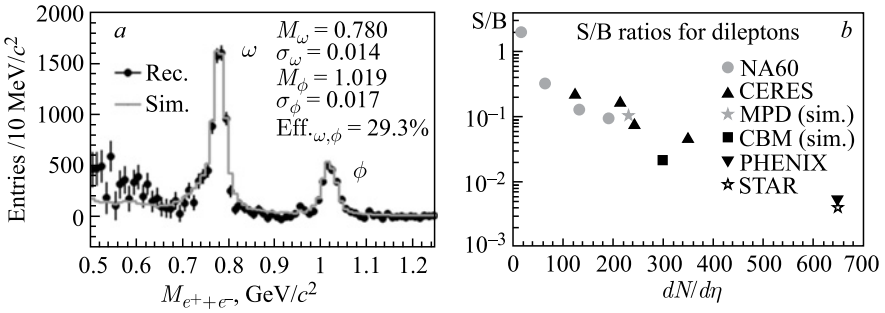

Fig. 28. *a*) Background-subtracted invariant mass distributions of electron–positron pairs from central Au + Au collisions at the MPD. *b*) Signal-to-Background (S/B) ratio from heavy-ion experiments as a function of total charged multiplicity

In Fig. 28, *a*, background-subtracted invariant mass distributions of electron–positron pairs in the pseudorapidity window $|\eta| < 1.0$ are plotted. A rough estimate of invariant mass resolution of the MPD setup was made by fitting the dileptons spectra at the poles for vector mesons: the RMS of 14 and 17 MeV was obtained for the ω- and ϕ-meson pole, respectively. The overall (integrated over the invariant mass window of $0.2{-}01.5$ GeV/c^2) signal-to-background ratio was found to be close to 10%. The obtained results for the signal-to-background ratio are shown in Fig. 28, *b*, along with the published data from other experiments. The expected parameters of the MPD setup are among the best over the world.

1.3. Study of Hyperon Production at NICA/MPD. Study of strangeness, in particular, hyperon production is of interest for several reasons. First, the theory predicts that the strangeness enhancement in heavy-ion-induced interactions (relative to elementary $p+p$ collisions) might be a signature for the deconfinement phase transition. The increase of the yield of strange particles in the QGP phase is due to both the lower threshold of the $s\overline{s}$-pair production and the addition of gluon fragmentation channels [71]. It was also observed in experiments that the enhancement is stronger for particles with higher strangeness content [72, 73].

Second, since the hadronic cross sections of multistrange hyperons are small, additional rescattering effects of hyperons in the dense nuclear matter are not as strong as for other hadrons. Thus, measured phase-space distributions of strange hyperons reveal important characteristics of the fireball at the early stages of the system evolution. Moreover, it has recently been observed by the STAR experiment that the characteristic azimuthal anisotropy pattern (e.g., the elliptic flow coefficient v_2 as a function of transverse momentum p_T) for antibaryons (including those with strangeness) is different from the one for baryons in mid-central Au + Au collisions at energies $\sqrt{s_{NN}} < 11$ GeV [74]. Due to an interplay between particle production and subsequent absorption in the medium the

antibaryons are strongly affected by the comoving baryon density in the course of the reaction. So, the outcome of the NICA program, in particular, new experimental data on (anti)hyperon production which will be taken with the MPD detector, will provide a valuable insight into the reaction dynamics and properties of the QCD matter.

The performance of the MPD detector for hyperon measurements was studied for a combination of the Time Projection Chamber (TPC) and the Time-Of-Flight system (TOF) covering the midrapidity region ($|\eta| < 1.3$). A small material budget (not exceeding 10% of the radiation length in the region of interest) and powerful particle ID based on the ionization loss (dE/dx) measurements in the TPC and time-of-flight information from the TOF allow precise trajectory reconstruction and reliable separation of particle species.

Hyperons and cascades were reconstructed using the secondary vertex finding technique with an optimized set of topological and track quality cuts as described in [75]. In Fig. 29 the invariant mass distributions of $\Lambda{-}\pi^-$ and $\Lambda{-}K^-$ pairs from central Au + Au collisions at the center-of-mass energy $\sqrt{s} = 9$ GeV are shown. The estimated efficiencies, Signal-to-Background (S/B) ratio and significance are also shown. Based on the results of this study, we have estimated the expected yields of particle species of interest for 10 weeks of the data taking at nominal NICA collider luminosities of $\approx 10^7$ and $\approx 10^6$ for Ξ^- and Ω^-, respectively. The accumulated statistics will allow one to get unique experimental information on the cascade production over a broad region of the QCD phase diagram and a large phase-space of the reaction.

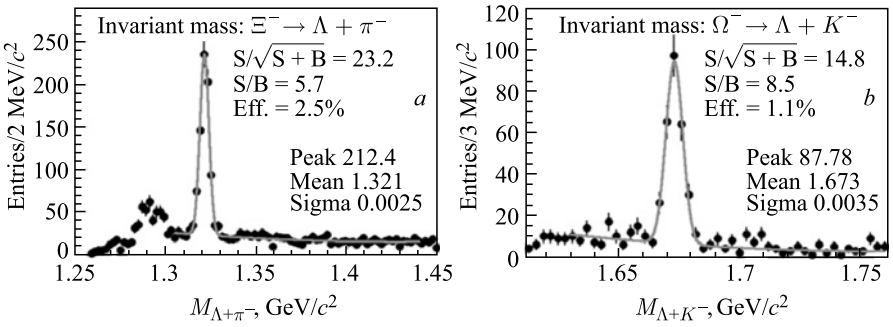

Fig. 29. The reconstructed invariant mass of Λ and π^- candidates (*a*), as well as of Λ and K^- pairs (*b*)

1.4. NICA/MPD Prospects in Hypernuclei Production. In relativistic heavy-ion collisions lots of strange particles (kaons and hyperons) are produced. Under such conditions, exotic nuclear objects with strangeness — hypernuclei [76,77] — can be formed. The search for hypernuclei offers the fascinating perspective to

explore the third (i.e., strange) axis of the nuclei chart. Moreover, the investigation of hypernuclei provides information on the hyperon–nucleon and even the hyperon–hyperon interactions, which plays an important role in the neutron star models. The mechanism and dynamics of hypernuclei formation are not well understood, and in order to distinguish between different models, new experimental data on hypernuclei production over large phase-space are required. The energy range of the NICA research program covers the region of the maximal baryon density where the production rates of nuclear clusters with strangeness are predicted to be enhanced considerably: as many as $3 \cdot 10^2$ of ${}^{3}_{\Lambda}\mathrm{H}$ and $1 \cdot 10^{-5}$ of ${}^{5}_{\Lambda\Lambda}\mathrm{He}$ per unit of rapidity are expected in a central $\mathrm{Au} + \mathrm{Au}$ collision at $\sqrt{s_{NN}} = 5$ GeV [78]. Here, we present the results of a study of the MPD capability for reconstruction of hypertritons. The analysis has been performed for $5 \cdot 10^5$ central events from the DCM–QGSM generator, corresponding to about 30 minutes of the data taking time at NICA. The full event reconstruction, realistic particle ID and secondary vertex finding have been performed as described in [75]. The obtained invariant mass spectra of helium-3 and π^- candidates are shown in Fig. 30.

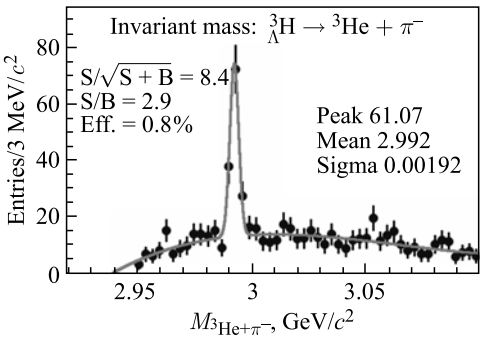

Fig. 30. The reconstructed invariant mass of ${}^{3}\mathrm{He}$ and π^- from central $\mathrm{Au} + \mathrm{Au}$ at $\sqrt{s} = 5A$ GeV

These results demonstrate a good sensitivity of the MPD setup for hypernuclei: with a typical event rate of 6 kHz for the NICA average luminosity of 10^{27} cm$^{-2} \cdot$ s^{-1} we will be able to register about 10^5 hypertritons in a week of the data taking. Thus, a detailed study of the production mechanism of single hypernuclei, as well as an observation of double hypernuclei at NICA, looks feasible.

2. PHYSICS STUDIES AT THE NUCLOTORON ENERGIES

Nucleus–nucleus collisions at the Nuclotron energies of up to 6 GeV per nucleon produce a fireball of the baryon densities in the collision zone of two gold nuclei exceeding the nuclear saturation density by a factor of $3-4$. Under such conditions, the participating nucleons start to overlap and the energy density is dominated by quarks occupying the Fermi sea and baryons representing the excited states. Due to the increase of the degrees of freedom with respect to the hadron gas, a new phase of nuclear matter of co-existing quark and baryonic matter — "quarkyonic" phase [79] — is predicted to be located in the region of large

baryochemical potentials and, thus, might be produced in the collisions of heavy ions at the Nuclotron. Moreover, the lattice QCD calculations suggest a deconfinement phase transition to occur at a critical energy density of ≈ 0.5 GeV/fm^3. Such energy densities are expected to be reached at the top Nuclotron energy in the fireball center. These conditions are well suited to investigate the EoS of dense nuclear matter, which plays a central role for the dynamics of core collapse supernovae and for the stability of neutron stars.

It is well known that the yields and the phase-space distributions of strange (Λ, Σ) and multistrange (Ξ, Ω) hyperons close to their production thresholds in the nucleon–nucleon collisions are sensitive to the properties and the degrees of freedom of the QCD matter at supernuclear densities. Due to multiple-step (or three-body) collisions involving Λ hyperons and kaons, the production of multistrange hyperons is expected to be enhanced at high densities, and their yield is sensitive to the baryon density reached in the fireball. Therefore, some systematic measurements of Ξ and Ω hyperon production as a function of the beam energy and size of the colliding nuclei offer a possibility to study the nuclear matter EoS at the Nuclotron.

While the properties of hadrons in the vacuum are at present well known, their characteristics (the masses and lifetimes) in a dense baryonic matter are a subject of current extensive research. In this context the modification of hadron properties, in particular, K mesons as well as vector (ρ, ω, ϕ) mesons in nuclear matter are of fundamental interest. The in-medium modification of kaon/antikaon properties can be explored experimentally in relativistic heavy-ion collisions at moderate bombarding energies; however, the existing experimental facilities are too limited in energy ($1.25A$ GeV is the highest energy presently available for Au + Au collisions at the SIS). One needs excitation functions for different symmetric systems, in which different densities are achieved. The Nuclotron provides a rich variety of beam species (up to gold) in a broad range of collision energies; therefore, it is ideally suited for this task.

At the same time, heavy-ion collisions reveal a rich source of strangeness, and the coalescence of kaons with Λ or Λ with nucleons will produce a vast variety of multistrange hyperons or light hypernuclei, respectively. Even the production of light double-hypernuclei or double-strange dibaryons is expected to be measured in heavy-ion collisions at the Nuclotron energies. The observation of those objects would represent a breakthrough in our understanding of strange matter and would pave a road for the experimental exploration of the third dimension of the nuclear chart.

The proposed design of the BM@N experiment was described in Introduction. Its tracker allows for having a precise momentum and vertex reconstruction, including secondary vertices. In addition, the design parameters of the time-of-flight detectors allow us to discriminate among hadrons (π, K, p) as well as identify light nuclei with the momentum of up to a few GeV/c. Here, we present

first results of feasibility study for the BM@N focusing on the efficiency of strange hyperons and hypernuclei measurements in central Au + Au collisions.

In Figs. 31 and 32, invariant mass of (Λ, π^-) and $({}^3\mathrm{He}, \pi^-)$ candidates, respectively, reconstructed with the GEM tracker from central lead–lead collisions at a beam kinetic energy of $4.5A$ GeV are shown. The obtained results indicate that the proposed setup has a reasonable reconstruction capability for strange hyperons produced in high-multiplicity events. The reconstructed signals of Ξ^- hyperon and hypertriton correspond to $9 \cdot 10^5$ and $2 \cdot 10^6$ central collisions, respectively. Taking into account the signal reconstruction efficiency, data acquisition capacity ($\approx$ 20 kHz of triggered events at the first stage of the BM@N experiment) and the duty factor of the Nuclotron beam, we expect to have for a month of the data taking a statistics of $2.7 \cdot 10^6$ and $4 \cdot 10^6$ for Ξ^- hyperons and hypertritons. This statistics is sufficient to perform a detailed experimental exploration of the strangeness production mechanism by measuring plenty of transverse momentum spectra, rapidity and angular distributions for hyperons and hypernuclei.

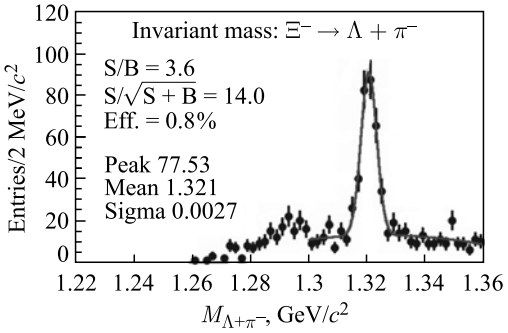

Fig. 31. Invariant mass of Λ and π^- candidates (BM@N)

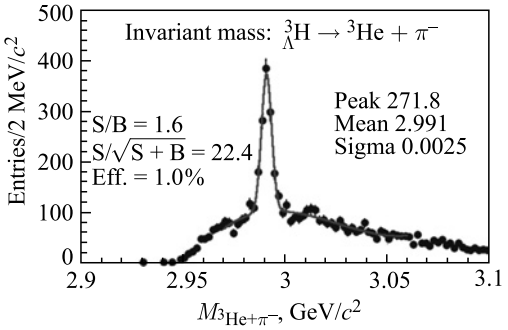

Fig. 32. Invariant mass of ^{3}He and π^- candidates (BM@N)

3. THE NICA WHITE PAPER PROPOSALS

We illustrate here the feasibility of the physics analysis which gives information on the bulk properties of the strongly interacting matter with the MPD and BM@N experiments and which is also carried out at the RHIC and SPS experiments. An overview over all the suggestions concerning observables to be measured with the NICA experiments has been collected in the NICA White Paper.

One of the phenomena, which was also simulated in the PHSD model, is an evidence for creation of the strong electromagnetic fields in asymmetric nuclear collisions. Due to difference in the number of protons of colliding nuclei, an electric field is generated and directed from the heavy to the light nucleus. This

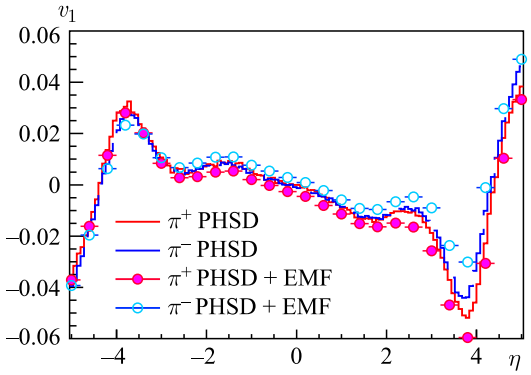

Fig. 33. Pseudorapidity dependence of direct flow of pions and K mesons created in off-central Cu + Au collisions at $\sqrt{s_{NN}} = 200$ GeV. The figure is taken from [80]

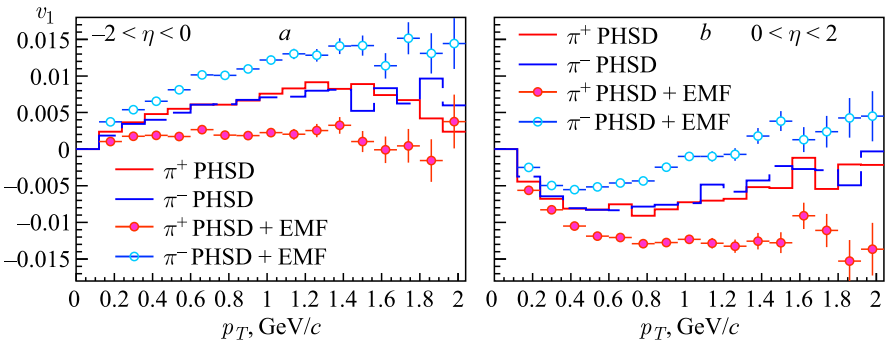

Fig. 34. Transverse momentum dependence of direct flow of $\pi^{\pm}$ produced in peripheral Cu + Au collisions for forward (b) and backward (a) emitted hadrons at $\sqrt{s_{NN}} = 200$ GeV. The figure is taken from [80]

strong electric field leads to a splitting of the direct flow v_1 for particles with the same mass but opposite electric charges [80]. This splitting for Cu + Au collisions at $\sqrt{s_{NN}} = 200$ GeV is shown in Figs. 33 and 34.

Here, the solid and dashed lines denote default calculations in the PHSD model; points correspond to incorporation of the electromagnetic field created in the collision. The effect is clearly seen on the transverse momentum distribution in Fig. 34.

At the NICA energies the magnitude of splitting effect should be the same, but value of direct flow is larger than at STAR. Presumably, NICA will be more preferable for this exploration.

Another very interesting suggestion discusses a possibility of experimental testing of signatures of P-odd effects related to the vorticity and hydrodynamic helicity of the medium [81, 82]. The studies of helicity and vorticity were performed within the framework of the kinetic Quark–Gluon String Model applied

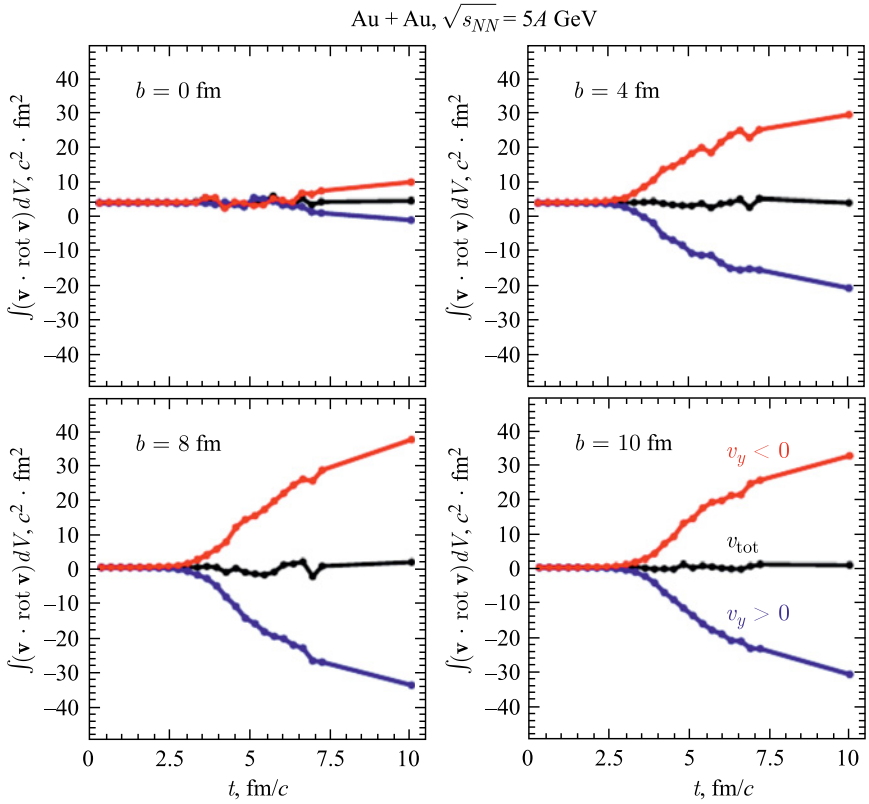

Fig. 35. Time dependence of helicity at different impact parameters

to the NICA kinematics. Figure 35 represents helicities in gold–gold collisions at different impact parameters evaluated in different domains. One can see that the helicity calculated with inclusion of all cells is equal to zero (middle line). For the cells with the definite sign of the velocity components, which are orthogonal to the reaction plane (which may also be selected experimentally), the helicity is nonzero and changes the sign for different signs of these components (upper and bottom lines, respectively). The effect is growing up with impact parameter and represents a sort of saturation in time. This effect of the helicity separation could be measured experimentally and is related to the global rotation of hadronic matter.

The NICA White Paper contains many other interesting suggestions for physics analysis in order to observe some effects which recent Monte Carlo generators cannot reproduce and then they could be verified with the real experimental data only.

4. SUMMARY

The experimental heavy-ion program at NICA will extend the study of reaction mechanisms and in-medium particle properties into an energy range that was formerly not accessible or where the experimental information was very poor. Nuclear collisions at the Nuclotron will create the net-baryon densities several times above the ground state. Although the first-principle theoretical calculations are not available for this energy domain, it has been speculated that the QCD phase diagram at high densities could have a rich structure. The exploration of matter under such conditions is thus of high physics interest. This situation underlines a necessity to perform the experiments at NICA because of the huge discovery potential in the low-temperature, high baryonic density domain of the QCD phase diagram.

The considered designs of the NICA experiments are well suited to provide a variety of experimental data for the critical assessments of the nuclear matter phase transition in the low-temperature and high baryonic density domain of the QCD phase diagram. The sophisticated theoretical models accompanied by results of a realistic Monte Carlo simulation of the proposed experimental setups at NICA support the ability of finding new phenomena in nuclei collisions.

Acknowledgements. The authors gratefully acknowledge all contributors of the NICA White Paper for their useful proposals to the NICA physics program and would especially like to thank Prof. R. Lednický for his helpful comments.

REFERENCES

1. NICA White Paper. http://nica.jinr.ru, free access.
2. *Arsene I. et al.* (*BRAHMS Collab.*). Quark–Gluon Plasma and Color Glass Condensate at RHIC? The Perspective from the BRAHMS Experiment // Nucl. Phys. A. 2005. V. 757, Nos. 1–2. P. 1–27.

3. *Back B. B. et al.* (*PHOBOS Collab.*). The Perspective on Discoveries at RHIC // Ibid. P. 28–101.
4. *Adams J. et al.* (*STAR Collab.*). Experimental and Theoretical Challenges in the Search for the Quark–Gluon Plasma: The STAR Collaboration's Critical Assessment of the Evidence from RHIC Collisions // Ibid. P. 102–183.
5. *Adcox K. et al.* (*PHENIX Collab.*). Formation of Dense Partonic Matter in Relativistic Nucleus–Nucleus Collisions at RHIC: Experimental Evaluation by the PHENIX Collaboration // Ibid. P. 184–283.
6. *Alt C. et al.* (*NA49 Collab.*). Pion and Kaon Production in Central Pb + Pb Collisions at 20A and 30A GeV: Evidence for the Onset of Deconfinement // Phys. Rev. C. 2008. V. 77. P. 024903.
7. *Abraamyan Kh. U. et al.* (*MPD Collab.*). The MPD Detector at the NICA Heavy-Ion Collider at JINR // Nucl. Instr. Meth. A. 2011. V. 628. P. 99–102.
8. *Poskanzer A. M., Voloshin S. A.* Methods for Analyzing Anisotropic Flow in Relativistic Nuclear Collisions // Phys. Rev. C. 1998. V. 58. P. 1671–1678.
9. *Adamczyk L. et al.* (*STAR Collab.*). Beam-Energy Dependence of the Directed Flow of Protons, Antiprotons, and Pions in Au + Au Collisions // Phys. Rev. Lett. 2014. V. 112, No. 16. P. 162301.
10. *Konchakovski V. P. et al.* Examination of the Directed Flow Puzzle in Heavy-Ion Collisions // Phys. Rev. C. 2014. V. 90, No. 1. P. 014903.
11. *Cassing W.* QCD Thermodynamics and Confinement from a Dynamical Quasiparticle Point of View // Nucl. Phys. A. 2007. V. 791. P. 365–381;
Cassing W., Bratkovskaya E. L. Parton Transport and Hadronization from the Dynamical Quasiparticle Point of View // Phys. Rev. C. 2008. V. 78. P. 034919;
Cassing W., Bratkovskaya E. L. Parton–Hadron-String Dynamics: An Off-Shell Transport Approach for Relativistic Energies // Nucl. Phys. A. 2009. V. 831. P. 215–242.
12. *Ivanov Yu. B., Russkikh V. N., Toneev V. D.* Relativistic Heavy-Ion Collisions within 3-Fluid Hydrodynamics: Hadronic Scenario // Phys. Rev. C. 2006. V. 73. P. 044904.
13. *Konchakovski V. P. et al.* Rise of Azimuthal Anisotropies as a Signature of the Quark–Gluon Plasma in Relativistic Heavy-Ion Collisions // Phys. Rev. C. 2012. V. 85. P. 011902.
14. *Cassing W., Bratkovskaya E. L.* Hadronic and Electromagnetic Probes of Hot and Dense Nuclear Matter // Phys. Rep. 1999. V. 308. P. 65–233.
15. *Bratkovskaya E. L., Cassing W., Stoecker H.* Open Charm and Charmonium Production at RHIC // Phys. Rev. C. 2003. V. 67. P. 054905.
16. *Bratkovskaya E. L. et al.* Strangeness Dynamics and Transverse Pressure in Relativistic Nucleus–Nucleus Collisions // Phys. Rev. C. 2004. V. 69. P. 054907.
17. *Linnyk O., Bratkovskaya E. L., Cassing W.* Open and Hidden Charm in Proton–Nucleus and Heavy-Ion Collisions // Intern. J. Mod. Phys. E. 2008. V. 17. P. 1367–1439.
18. *Konchakovski V. P. et al.* Fluctuations and Correlations in Nucleus–Nucleus Collisions within Transport Models // J. Phys. G. 2010. V. 37. P. 073101.
19. *Bratkovskaya E. L., Cassing W., Linnyk O.* Low Mass Dilepton Production at Ultrarelativistic Energies // Phys. Lett. B. 2009. V. 670. P. 428–433.

20. *Wang G.* Correlations Relative to the Reaction Plane at the Relativistic Heavy Ion Collider Based on Transverse Deflection of Spectator Neutrons. Ph. D. Thesis. Kent State Univ., 2006.
21. *Kharzeev D.* Parity Violation in Hot QCD: Why It Can Happen, and How to Look for It // Phys. Lett. B. 2006. V. 633. P. 260–264.
22. *Voloshin S. A.* Probe for the Strong Parity Violation Effects at RHIC with Three Particle Correlations // Ind. J. Phys. 2011. V. 85. P. 1103–1107.
23. *Kharzeev D. E., McLerran L. D., Warringa H. J.* The Effects of Topological Charge Change in Heavy Ion Collisions: "Event by Event P and CP Violation" // Nucl. Phys. A. 2008. V. 803. P. 227–253.
24. *Skokov V., Illarionov A. Yu., Toneev V.* Estimate of the Magnetic Field Strength in Heavy-Ion Collisions // Intern. J. Mod. Phys. A. 2009. V. 24. P. 5925–5932.
25. *Voronyuk V. et al.* (Electro-)Magnetic Field Evolution in Relativistic Heavy-Ion Collisions // Phys. Rev. C. 2011. V. 83. P. 054911.
26. *Voloshin S. A.* Parity Violation in Hot QCD: How to Detect It // Phys. Rev. C. 2004. V. 70. P. 057901.
27. *Adamczyk L. et al.* (*STAR Collab.*). Beam-Energy Dependence of Charge Separation along the Magnetic Field in Au + Au Collisions at RHIC // Phys. Rev. Lett. 2014. V. 113. P. 052302.
28. *Bzdak A., Koch V., Liao J.* Remarks on Possible Local Parity Violation in Heavy Ion Collisions // Phys. Rev. C. 2010. V. 81. P. 031901.
29. *Toneev V. D. et al.* Theoretical Analysis of a Possible Observation of the Chiral Magnetic Effect in Au + Au Collisions within the RHIC Beam Energy Scan Program // Phys. Rev. C. 2012. V. 85. P. 034910.
30. *Toneev V. D. et al.* Event-by-Event Background in Estimates of the Chiral Magnetic Effect // Ibid. V. 86. P. 064907.
31. *Ivanov Yu. B.* Alternative Scenarios of Relativistic Heavy-Ion Collisions: I. Baryon Stopping // Phys. Rev. C. 2013. V. 87, No. 6. P. 064904.
32. *Cleymans J.* Maximal Net Baryon Density in the Energy Region Covered by NICA // Phys. Part. Nucl. Lett. 2011. V. 8. P. 6–10.
33. *Appelshauser H. et al.* (*NA49 Collab.*). Baryon Stopping and Charged Particle Distributions in Central Pb + Pb Collisions at 158 GeV per Nucleon // Phys. Rev. Lett. 1999. V. 82. P. 2471–2475.
34. *Ivanov Yu. B.* Alternative Scenarios of Relativistic Heavy-Ion Collisions: II. Particle Production // Phys. Rev. C. 2013. V. 87, No. 6. P. 064905.
35. *Karpenko Iu. A. et al.* Estimation of the Shear Viscosity at Finite Net-Baryon Density from $A + A$ Collision Data at $\sqrt{s_{NN}} = 7.7-200$ GeV // Phys. Rev. C. 2015. V. 91, No. 6. P. 064901.
36. *Podgoretsky M. I.* Interference Correlations of Identical Pions: Theory // Part. Nucl. 1989. V. 20. P. 628–668 (in Russian).
37. *Lorstad B.* Boson Interferometry — A Review of High-Energy Data and Its Interpretation // Intern. J. Mod. Phys. A. 1989. V. 4. P. 2861–2896.
38. *Boal D. H., Gelbke C. K., Jennings B. K.* Intensity Interferometry in Subatomic Physics // Rev. Mod. Phys. 1990. V. 62. P. 553–602.

39. *Wiedemann U. A., Heinz U. W.* Particle Interferometry for Relativistic Heavy Ion Collisions // Phys. Rep. 1999. V. 319. P. 145–230.
40. *Csorgo T.* Particle Interferometry from 40 MeV to 40 TeV // Heavy Ion Phys. 2002. V. 15. P. 1–80.
41. *Lednicky R.* Correlation Femtoscopy of Multiparticle Processes // Phys. At. Nucl. 2004. V. 67. P. 72–82 (Yad. Fiz. 2004. V. 67. P. 73).
42. *Lisa M. A. et al.* Femtoscopy in Relativistic Heavy Ion Collisions // Ann. Rev. Nucl. Part. Sci. 2005. V. 55. P. 357–402.
43. *Lednicky R., Lyuboshitz V. L.* Influence of Final State Interaction on Correlations of Two Particles with Nearly Equal Momenta // Sov. J. Nucl. Phys. 1982. V. 35. P. 770.
44. *Podgoretsky M. I.* On the Comparison of Identical Pion Correlations in Different Reference Frames // Sov. J. Nucl. Phys. 1983. V. 37. P. 272.
45. *Csorgo T., Pratt S.* Structure of the Peak in Bose–Einstein Correlations // Proc. of the Conf. on Relativistic Heavy-Ion Phys. at Present and Future Accelerators, Budapest, 1991. P. 75.
46. *Rischke D. H., Gyulassy M.* The Time Delay Signature of Quark–Gluon Plasma Formation in Relativistic Nuclear Collisions // Nucl. Phys. A. 1996. V. 608. P. 479–512.
47. *Antinori F. et al.* (*WA97 Collab.*). Centrality Dependence of the Expansion Dynamics in PbPb Collisions at 158-A-GeV/c // J. Phys. G. 2001. V. 27. P. 2325–2344.
48. *Lisa M. A. et al.* (*E895 Collab.*). Bombarding Energy Dependence of π^- Interferometry at the Brookhaven AGS // Phys. Rev. Lett. 2000. V. 84. P. 2798–2802.
49. *Ahle L. et al.* (*E802 Collab.*). System, Centrality, and Transverse Mass Dependence of Two Pion Correlation Radii in Heavy Ion Collisions at 11.6-A-GeV and 14.6-A-GeV // Phys. Rev. C. 2002. V. 66. P. 054906.
50. *Kniege S. et al.* (*NA49 Collab.*). Rapidity and Transverse Momentum Dependence of $\pi^-\pi^-$ Bose–Einstein Correlations Measured at 20-A-GeV, 30-A-GeV, 40-A-GeV, 80-A-GeV and 158-A-GeV Beam Energy // J. Phys. G. 2004. V. 30. P. S1073–S1078.
51. *Adamova D. et al.* (*CERES Collab.*). Beam Energy and Centrality Dependence of Two Pion Bose–Einstein Correlations at SPS Energies // Nucl. Phys. A. 2003. V. 714. P. 124–144.
52. *Adler S. S. et al.* (*PHENIX Collab.*). Bose–Einstein Correlations of Charged Pion Pairs in Au + Au Collisions at $\sqrt{s_{NN}} = 200$ GeV // Phys. Rev. Lett. 2004. V. 93. P. 152302.
53. *Adcox K. et al.* (*PHENIX Collab.*). Transverse Mass Dependence of Two Pion Correlations in Au + Au Collisions at $\sqrt{s_{NN}} = 130$ GeV // Phys. Rev. Lett. 2002. V. 88. P. 192302.
54. *Back B. B. et al.* (*PHOBOS Collab.*). Transverse Momentum and Rapidity Dependence of HBT Correlations in Au + Au Collisions at $\sqrt{s_{NN}} = 62.4$ GeV and 200 GeV // Phys. Rev. C. 2006. V. 73. P. 031901.
55. *Adler C. et al.* (*STAR Collab.*). Pion Interferometry of $\sqrt{s_{NN}} = 130$ GeV Au + Au Collisions at RHIC // Phys. Rev. Lett. 2001. V. 87. P. 082301.
56. *Adams J. et al.* (*STAR Collab.*). Pion Interferometry in Au + Au Collisions at $\sqrt{s_{NN}} =$ 200 GeV // Phys. Rev. C. 2005. V. 71. P. 044906.

57. *Florkowski W. et al.* Hydrodynamics and Perfect Fluids: Uniform Description of Soft Observables in Au + Au Collisions at RHIC // Proc. of the 38th Intern. Symp. on Multiparticle Dynamics (ISMD08). 2008. P. 109–113.
58. *Pratt S.* Resolving the HBT Puzzle in Relativistic Heavy Ion Collision // Phys. Rev. Lett. 2009. V. 102. P. 232301.
59. *Stephanov M. A.* QCD Phase Diagram and the Critical Point // Prog. Theor. Phys. Suppl. 2004. V. 153. P. 139–156 (Intern. J. Mod. Phys. A. 2005. V. 20. P. 4387).
60. *Lednicky R.* Femtoscopic Search for the Phase Transition // Nucl. Phys. Proc. Suppl. 2010. V. 198. P. 43–45.
61. *Chajecki Z. et al.* AA versus PP (and dA): A Puzzling Scaling in NBT and RHIC // Proc. of the 21st Winter Workshop on Nucl. Dynamics. 2005.
62. *Lednický R. et al.* How to Measure Which Sort of Particles Was Emitted Earlier and Which Later? // Phys. Lett. B. 1996. V. 373, Nos. 1–3. P. 30–34.
63. *Graczykowski L. K.* Pion Femtoscopy Measurements in ALICE at the LHC // EPJ Web Conf. 2014. V. 71. P. 00051.
64. *Brown D., Danielewicz P.* Imaging of Sources in Heavy-Ion Collisions // Phys. Lett. B. 1997. V. 398. P. 252–258.
65. *Brown D., Danielewicz P.* Optimized Discretization of Sources Imaged in Heavy Ion Reactions // Phys. Rev. C. 1998. V. 57. P. 2474–2483.
66. *Hatsuda T., Lee S. H.* QCD Sum Rules for Vector Mesons in Nuclear Medium // Phys. Rev. C. 1992. V. 46. P. 34–38.
67. *Rapp R., Chanfray G., Wambach J.* Medium Modifications of the ρ Meson at CERN SPS Energies // Phys. Rev. Lett. 1996. V. 76. P. 368–371.
68. *Brown G. E., Rho M.* Scaling Effective Lagrangians in a Dense Medium // Phys. Rev. Lett. 1991. V. 66. P. 2720–2723.
69. *Randrup J., Cleymans J.* Maximum Freeze-Out Baryon Density in Nuclear Collisions // Phys. Rev. C. 2006. V. 74. P. 047901.
70. *Vasendina V. et al.* Study of the MPD Detector Capabilities for Electron–Positron Pair Measurements at the NICA Collider // Phys. Part. Nucl. Lett. 2013. V. 10, No. 7. P. 769–777.
71. *Rafelski J., Muller B.* Strangeness Production in the Quark–Gluon Plasma // Phys. Rev. Lett. 1982. V. 48. P. 1066; Erratum // Phys. Rev. Lett. 1986. V. 56. P. 2334.
72. *Antinori F. et al.* (*WA97 Collab.*). Strangeness Enhancement at Midrapidity in Pb Pb Collisions at 158-A-GeV/c: A Comparison with VENUS and RQMD Models // Eur. Phys. J. C. 1999. V. 11. P. 79–88.
73. *Antinori F. et al.* (*NA57 Collab.*). Enhancement of Hyperon Production at Central Rapidity in 158-A-GeV/c Pb–Pb Collisions // J. Phys. G. 2006. V. 32. P. 427–442.
74. *Adamczyk L. et al.* (*STAR Collab.*). Elliptic Flow of Identified Hadrons in Au + Au Collisions at $\sqrt{s_{NN}} = 7.7-62.4$ GeV // Phys. Rev. C. 2013. V. 88. P. 014902.
75. *Ilieva M. et al.* Evaluation of the MPD Detector Capabilities for the Study of the Strangeness Production at the NICA Collider // Phys. Part. Nucl. Lett. 2015. V. 12, No. 1. P. 100–112.
76. *Kerman A. K., Weiss M. S.* Superstrange Nuclei // Phys. Rev. C. 1973. V. 8. P. 408–410.

77. *Abelev B. I.* Observation of an Antimatter Hypernucleus // Science. 2010. V. 328. P. 58–62.
78. *Andronic A. et al.* Production of Light Nuclei, Hypernuclei and Their Antiparticles in Relativistic Nuclear Collisions // Phys. Lett. B. 2011. V. 697. P. 203–207.
79. *McLerran L., Pisarski R. D.* Phases of Cold, Dense Quarks at Large $N(c)$ // Nucl. Phys. A. 2007. V. 796. P. 83–100.
80. *Voronyuk V. et al.* Charge-Dependent Directed Flow in Asymmetric Nuclear Collisions // Phys. Rev. C. 2014. V. 90, No. 6. P. 064903.
81. *Rogachevsky O. V., Sorin A. S., Teryaev O. V.* Chiral Vortaic Effect and Neutron Asymmetries in Heavy-Ion Collisions // Phys. Rev. C. 2010. V. 82. P. 054910.
82. *Baznat M. et al.* Helicity Separation in Heavy-Ion Collisions // Phys. Rev. C. 2013. V. 88. P. 061901.